The Astrophysical Journal, 998:260 (30pp), 2026 February 20 https://doi.org/10.3847/1538-4357/ae2ea4

The Major Solar Energetic Particle Event on 2024 May 20: Multispacecraft Observations of a Long-lasting Energetic Particle Reservoir

D. Lario[1], J. Hu[1,2], L. A. Balmaceda[1,3], R. Y. Kwon[4], S. Wallace[5], D. E. da Silva[1,6], M. L. Mays[1], V. Krupar[1,6], F. Carcaboso[1,6], A. Warmuth[7], M. Z. Stiefel[8], L. Y. Khoo[9], I. G. Richardson[1,10], P. Kühl[11], R. F. Wimmer-Schweingruber[11], R. Vainio[12], E. Riihonen[12], W. Liu[13], A. Aran[14], E. Paouris[15], M. R. Kane[1,16], C. O. Lee[17], C. Sasso[18], C. N. Arge[1], S. I. Jones[1,16], J. Verniero[1], A. E. Niemela[1,6], T. S. Horbury[19], and M. Maksimovic[20]

[1] Heliophysics Science Division, NASA Goddard Space Flight Center, Greenbelt, MD, USA; david.larioloyo@nasa.gov
[2] Department of Space Science and CSPAR, University of Alabama in Huntsville, Huntsville, AL, USA
[3] Physics and Astronomy Department, George Mason University, 4400 University Drive, Fairfax, VA 22030, USA
[4] Korea Astronomy and Space Science Institute, Daedeokdae-ro 776, Yuseong-gu, Daejeon 34055, Republic of Korea
[5] Embry-Riddle Aeronautical University, 1 Aerospace Boulevard, Daytona Beach, FL 32114, USA
[6] Goddard Planetary Heliophysics Institute, University of Maryland, Baltimore County, Baltimore, MD 21250, USA
[7] Leibniz-Institut für Astrophysik Potsdam (AIP), An der Sternwarte 16, 14482 Potsdam, Germany
[8] University of Applied Sciences and Arts Northwestern Switzerland, Bahnhofstrasse 6, 5210 Windisch, Switzerland
[9] Department of Astrophysical Sciences, Princeton University, Princeton, NJ 08544, USA
[10] Department of Astronomy, University of Maryland, College Park, MD 20742, USA
[11] Institute of Experimental and Applied Physics, Christian-ALbrechts-University Kiel, 24118 Kiel, Germany
[12] Department of Physics and Astronomy, University of Turku, FI-20014 Turku, Finland
[13] Department of Climate and Space Sciences and Engineering, University of Michigan, Ann Arbor, MI 48109, USA
[14] Department of Quantum Physics and Astrophysics, Institute of Cosmos Sciences (ICCUB), Universitat de Barcelona (UB-IEEC), Spain
[15] The Johns Hopkins University Applied Physics Laboratory, 11100, Johns Hopkins Road, Laurel, MD 20723, USA
[16] Catholic University of America, 620 Michigan Avenue, N.E. Washington, DC 20064, USA
[17] Space Sciences Lab, University of California Berkeley, Berkeley, CA 94720, USA
[18] National Institute for Astrophysics, Astronomical Observatory of Capodimonte, Salita Moiariello 16, I-80131 Napoli, Italy
[19] The Blackett Laboratory, Imperial College London, London SW72AZ, UK
[20] LIRA, Observatoire de Paris, Université PSL, CNRS, Sorbonne Université, Université de Paris, F-92195 Meudon, France
Received 2025 October 20; revised 2025 December 10; accepted 2025 December 15; published 2026 February 13

Abstract

The fleet of spacecraft distributed across the inner heliosphere during 2024 May–June provided a unique opportunity to analyze, over a broad range of heliolongitudes, the effects produced by the complex sunspot group associated with Active Region 13664. The intense solar activity from 2024 May 8 to 2024 June 21 produced unusually elevated solar energetic particle (SEP) intensities observed at heliocentric distances $\lesssim$1 au by Solar Orbiter, Parker Solar Probe, STEREO-A, and near-Earth spacecraft. This activity resulted in a >40 day period of enhanced $\lesssim$10 MeV proton intensities spanning at least $\sim$170° in longitude. Among these events, the 2024 May 20 SEP event was remarkable for its high intensity and wide spatial extent. It was associated with a fast ($\gtrsim$1500 km s^{-1}) halo coronal mass ejection (CME) and an X16.5 solar flare located $\sim$171° in longitude from Earth. Near Earth, the event produced a long-lasting $\sim$100 MeV proton intensity enhancement with energy spectra flattening between 30 and 80 MeV. It also led to the formation of an energetic particle reservoir that persisted for $\sim$2 weeks and extended across at least $\sim$170° in longitude. Several mechanisms contributed to the broad longitudinal spread of SEPs and formation of the energetic particle reservoir, including acceleration at an extended CME-driven shock, particle drifts along the heliospheric current sheet, particle reflection and redistribution caused by the merging of preceding CMEs beyond 1 au, and predominantly cross-field particle transport processes.

Unified Astronomy Thesaurus concepts: Solar physics (1476); Solar energetic particles (1491); Interplanetary physics (827); Solar coronal mass ejection shocks (1997)

1. Introduction

Solar eruptions, in the form of solar flares, narrow coronal jets, or broad coronal mass ejections (CMEs), are often accompanied by solar energetic particle (SEP) intensity enhancements observed by spacecraft in interplanetary (IP) space (e.g., H. Kunow et al. 1991; D. V. Reames 1999, 2021). The observation of SEP events at widely separated heliospheric locations has long raised questions about the mechanisms responsible for the spread of particles in the heliosphere (e.g., R. Gómez-Herrero et al. 2015; D. Lario et al. 2017b, 2017a; D. V. Reames 2023; and references therein). Mechanisms proposed in the literature include (1) broad particle sources associated with coronal and IP shocks initially driven by CMEs capable of accelerating and injecting particles over a wide range of heliolongitudes (e.g., E. W. Cliver et al. 1995, 2005; and references therein), (2) cross-field transport processes in the corona and/or IP space enabling particles injected from narrow solar sources to spread widely in the heliosphere (e.g., M. Zhang et al. 2009; W. Dröge et al. 2010, 2016; N. Dresing et al. 2012; and references therein), (3) efficient drift transport processes along the heliospheric current sheet (HCS; e.g., A. Moradi & J. Giacalone 2025; C. O. G. Waterfall et al. 2025), and (4) complex magnetic field configurations in the corona and/or IP

space that allow SEPs injected from narrow sources to reach distant heliospheric locations (e.g., K. L. Klein et al. 2008; S. Masson et al. 2012, 2013).

The acceleration of particles by CME-driven shocks provides a natural explanation for the observation of SEP events over a wide range of heliolongitudes (e.g., H. V. Cane et al. 1988). This requires that, in the absence of SEP transport across field lines, (1) the shock establishes magnetic connection with those spacecraft that observe SEPs as it expands through the corona and IP space, (2) the regions of the shock magnetically connected to each spacecraft provide the conditions necessary for an efficient acceleration and injection of particles onto the magnetic field lines connecting to each spacecraft, and (3) SEPs propagate along these field lines before reaching the observing spacecraft (e.g., H. V. Cane et al. 1988; D. Lario et al. 1998; W. Liu et al. 2025). However, the detection of SEPs by spacecraft poorly magnetically connected with the CME-driven shocks led to alternative hypotheses invoking cross-field transport processes (e.g., M. Zhang et al. 2009; W. Dröge et al. 2010, 2016; N. Dresing et al. 2012; D. Lario et al. 2014, 2017b; A. Kollhoff et al. 2021; M. Zhang et al. 2023; A. Posner et al. 2024), and/or particle drifts along the HCS structure (e.g., A. Moradi & J. Giacalone 2025; C. O. G. Waterfall et al. 2025) as mechanisms to spread SEPs through the inner heliosphere. Uncertainties in estimating both the spacecraft magnetic connectivity to the particle sources (e.g., D. Lario et al. 2017a; and references therein), the extent and properties of the CME-driven shocks as particle accelerators (e.g., D. Lario et al. 2017b), and the actual HCS structure (C. O. G. Waterfall et al. 2025) limit our ability to quantify the relative contributions that extended particle sources and/or transport processes have in spreading SEPs throughout the heliosphere.

The observation of remarkably similar particle intensities and energy spectra during the decay phase of large SEP events by spacecraft widely separated in longitude, latitude, and radial distance also raised questions about the SEP transport processes in the heliosphere (R. B. McKibben 1972; E. C. Roelof et al. 1992; D. V. Reames et al. 1996, 1997; D. Lario et al. 2003; R. B. McKibben et al. 2003; D. Lario et al. 2006; D. Lario 2010; H. Q. He 2021; D. V. Reames 2023; Y. Wang & G. Qin 2023). These periods have been commonly termed energetic particle reservoirs (e.g., E. C. Roelof et al. 1992). The mechanisms proposed in the literature to explain the global filling of the inner heliosphere with nearly equal particle intensities evolving similarly in time after the occurrence of an SEP event invoke either (i) effective field-aligned and cross-field transport processes (e.g., Y. Wang & G. Qin 2023), (ii) shielding effects by preevent plasma structures formed beyond the spacecraft locations able to both reflect and redistribute particles to inner heliospheric distances (E. C. Roelof et al. 1992), or (iii) confinement of particles behind the CME-driven shock responsible for the origin of the SEP event (D. V. Reames et al. 1996). Successive SEP injections by a sequence of solar eruptions from either an extremely active region (AR) or a combination of several ARs may also result in a global filling of the heliosphere, although the nearly equal particle intensities evolving similarly in time are more difficult to observe (R. B. McKibben et al. 2003; D. Lario et al. 2003; D. Lario 2010).

The fleet of spacecraft distributed in the inner ($\lesssim$1 au) heliosphere during 2024 May–June (see Section 2 below) offered us an excellent opportunity to analyze these SEP phenomena. In early 2024 May, a sequence of emerging magnetic structures near the National Oceanic and Atmospheric Administration (NOAA) AR 13664 formed a large and complex photospheric magnetic configuration (I. Kontogiannis 2024; Y.-S. Kwak et al. 2024; M. Dikpati et al. 2025) that, as it transited over the Earth-facing side of the Sun, produced a substantial number of M- and X-class X-ray solar flares and CMEs that impacted the Earth's environment (e.g., N. M. Kondrashova et al. 2024; O. Kruparova et al. 2024; Y. Li et al. 2024; P. Romano et al. 2024; H. Hayakawa et al. 2025; A. Razquin et al. 2025). The evolution of this complex AR structure (abbreviated to AR 13664) and the role that this structure played in the production of flares and CMEs as it transited over the Earth-facing side of the Sun can be found elsewhere (e.g., R. Jarolim et al. 2024; I. Kontogiannis 2024; P. Jaswal et al. 2025; D. MacTaggart et al. 2025). From Earth's point of view, it was possible to track this AR over at least three consecutive solar rotations (e.g., N. M. Kondrashova et al. 2024): (i) from 2024 April 30 when it appeared over the east limb of the Sun, developed into a highly complex magnetic structure on 2024 May 4–10, and rotated beyond the west limb on 2024 May 14, (ii) from 2024 May 28 to June 10 when it reappeared on the Earth-facing side of the Sun (with the new number AR 13697 and a less compact structure), and (iii) from 2024 June 23 to July 5 as a disaggregated AR complex (with the AR numbers 13723, 13727, and 13728). During this period, Solar Orbiter (SolO; D. Müller et al. 2020) was nearly diametrically opposite to Earth with respect to the Sun, offering a global coverage to continuously track the AR even on the far side of the Sun (C. Blinder 2025; I. Kontogiannis et al. 2025). Effects of this AR complex in terms of SEPs included the generation of two ground-level enhancements (GLEs); specifically GLE-74 on 2024 May 11 (A. Papaioannou et al. 2025), and GLE-75 on 2024 June 8 (S. Poluianov et al. 2025). In this paper, we analyze the energetic particle environment of the inner heliosphere during the period 2024 May–June using measurements from SolO, Parker Solar Probe (PSP; N. J. Fox et al. 2016), the spacecraft Ahead of the Solar TErrestrial RElations Observatory (STA; M. L. Kaiser et al. 2008), and spacecraft at the Sun–Earth Lagrangian point L1 such as the Solar and Heliospheric Observatory (SOHO; V. Domingo et al. 1995), the Advanced Composition Explorer (ACE; E. C. Stone et al. 1998), and the Wind spacecraft (M. H. Acuña et al. 1995; R. Harten & K. Clark 1995), together with the near-Earth Geostationary Operational Environmental Satellite #16 (GOES-16).[21]

The structure of the paper is as follows. Section 2 describes the spacecraft location and used datasets. Section 3 describes energetic particle observations throughout the period 2024 May–June, comparing particle intensities measured at PSP, SolO, STA, and L1, paying special attention to the most energetic SEP events. We identify the fastest ($\gtrsim$800 km s^{-1}) CMEs and most intense (X-ray class $\geqslant$ M5.0) flares occurring during this period, and highlight the most intense X-ray solar flare; i.e., an X16.5 class flare with onset at 05:12 UT on 2024 May 20 observed at Stonyhurst coordinates S19W171. Section 4 focuses on the most intense SEP event during the 2024 May–June period as observed by both PSP and SolO. The origin of this SEP event was associated with a fast halo CME temporally associated with the X16.5 flare on 2024 May 20. This SEP event had the peculiarity of creating a long-lasting

[21] https://www.ncei.noaa.gov/products/satellite/goes-r

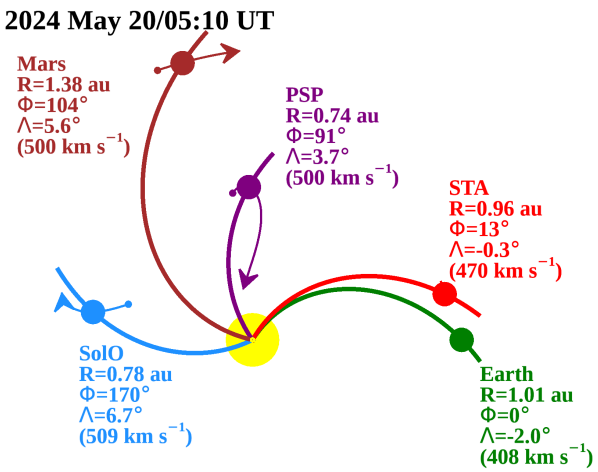

Figure 1. Schematic representation of the nominal interplanetary magnetic field configuration in the solar equatorial plane as seen from the north, showing field lines connecting the Sun to the locations of Earth (green circle), Solar Orbiter (SolO; blue circle), STEREO-A (STA; red circle), Parker Solar Probe (PSP; purple circle), and Mars (brown circle) on 2024 May 20 at 05:10 UT. Nominal Parker spiral magnetic field lines have been plotted using the solar wind speed indicated next to the HEEQ coordinates of each spacecraft; R being the heliocentric radial distance, Φ the HEEQ longitude, and Λ the latitude. The thin lines passing by SolO, PSP, and Mars locations indicate the trajectory of these objects from 2024 May 4 (small dots) to 2024 June 24 (arrows).

($\gtrsim$2 week) energetic particle reservoir observed over at least a span of $\sim$170° in longitude; whereas high-energy ($\gtrsim$100 MeV) protons were observed near Earth with a proton energy spectrum flattening over the energy range $\sim$30–80 MeV. The arrival of $>$100 MeV protons at Earth during this event provides an exceptional case study to investigate the main mechanisms contributing to the spread of SEPs in the inner heliosphere as described in Section 5. Finally, Section 6 summarizes the main conclusions of this work regarding the spreading of SEPs during this intense period of activity.

2. Spacecraft Distribution and Used Datasets

Figure 1 shows the spatial distribution of the spacecraft from which we use observations. The filled circles (not to scale) indicate the locations of the Sun (yellow), STA (red), SolO (blue), PSP (purple), and Earth (green) in the solar equatorial plane as seen from the north. We also indicate as a reference the location of Mars (brown). The legend next to each symbol provides the heliocentric radial distance R, and the Heliocentric Earth Equatorial (HEEQ) longitude Φ and latitude Λ of each location on 2024 May 20 at 05:10 UT. Nominal magnetic field lines connecting each one of these locations with the Sun are shown assuming a Parker spiral magnetic field configuration with the solar wind speed indicated in the legend next to each symbol. From 2024 May 4 to 2024 June 24 (the period analyzed in this paper), the different spacecraft moved from the location indicated by the small dot to the location indicated by the arrow along their respective trajectories. In particular, SolO moved outward from the Sun from $R = 0.62$ au and $\Phi = 164°$ on 2024 May 4 to $R = 0.95$ au and $\Phi = 167°$ on 2024 June 24, passing $\Phi = 170°$ on 2024 May 20. On 2024 May 4, PSP was at $R = 0.72$ au and $\Phi = 98°$, reached its aphelion at $R = 0.74$ au and $\Phi = 93°$ on 2024 May 15, and by 2024 June 24 was at $R = 0.28$ au and $\Phi = 96°$ directed toward its perihelion #20. During this period, STA was at $R \sim 0.96$ au and moving westward relative to Earth from $\Phi = 12°$ to $\Phi = 17°$. Mars was at $R \sim 1.39$ au, and moving from $\Phi = 109°$ on 2024 May 4 to $\Phi = 93°$ on 2024 June 24.

The remote-sensing instruments on board SolO, STA, and near-Earth spacecraft such as GOES-16, the Solar Dynamics Observatory (SDO; W. D. Pesnell et al. 2012), and SOHO allowed us to continuously track AR 13664. In particular, the Full Disk Telescope of the Polarimetric and Helioseismic Imager (PHI; S. K. Solanki et al. 2020), the Full-Sun Imager (FSI) of the Extreme Ultraviolet Imager (SolO/EUI/FSI; P. Rochus et al. 2020), and the Spectrometer Telescope for Imaging X-rays (STIX; S. Krucker et al. 2020) on board SolO allowed us to follow the location and activity produced by AR 13664 when located on the far side of the Sun as seen from Earth. X-ray observations from the X-ray Sensor (XRS; P. C. Chamberlin et al. 2009) on board GOES-16, extreme ultraviolet (EUV) observations from the Atmospheric Imaging Assembly (AIA; J. R. Lemen et al. 2012) on SDO, and white-light (WL) CME observations from the Large Angle Spectroscopic Coronagraph (LASCO; G. E. Brueckner et al. 1995) on SOHO enabled the tracking of AR 13664 and its activity as seen from Earth. From the point of view of STA, we use EUV images from the Extreme UltraViolet Imager (EUVI; J.-P. Wuelser et al. 2004), and WL images of CMEs from the coronagraphs COR1 and COR2 of the Sun Earth Connection Coronal and Heliospheric Investigation (R. A. Howard et al. 2008).

In terms of energetic particle data, we combine measurements from the Energetic Particle Detector suite of instruments on board SolO (EPD; J. Rodríguez-Pacheco et al. 2020); the Energetic Particle Instruments (EPI)-Lo and EPI-Hi of the Integrated Science Investigation of the Sun (IS$\odot$IS; D. J. McComas et al. 2016) on board PSP; the Solar Electron and Proton Telescope (SEPT; R. Müller-Mellin et al. 2008) and STA/High Energy Telescope (HET; T. T. von Rosenvinge et al. 2008) of the in situ Measurements of Particles and CME Transients (J. G. Luhmann et al. 2008) suite of instruments on board STA; the Low-Energy Magnetic Spectrometer (LEMS120) and the Deflected Electron (DE) system of the Electron, Proton, and Alpha Monitor (EPAM; R. E. Gold et al. 1998) on board ACE; the Electron Proton Helium Instrument (EPHIN; R. Müller-Mellin et al. 1995) on board SOHO; the High Energy Detector (HED) of the Energetic and Relativistic Nuclei and Electron (ERNE; J. Torsti et al. 1995) experiment on board SOHO; and the Solar and Galactic Proton Sensor (SGPS; B. T. Kress et al. 2021) of the Space Environment In Situ Suite on board GOES-16.

In order to investigate the radio bursts associated with these SEP events, we use radio observations by the FIELDS instrument on PSP (S. D. Bale et al. 2016), the Radio and Plasma Waves (RPW) instrument on board SolO (M. Maksimovic et al. 2020), the Radio and Plasma Wave Investigations on both STA (SWAVES; J. L. Bougeret et al. 2008) and the Wind spacecraft (WAVES; J. L. Bougeret et al. 1995). In order to identify the arrival of solar wind structures at each spacecraft, we use magnetic field observations by the magnetometers (MAG) on board SolO (T. S. Horbury et al. 2020), ACE (ACE/MAG; C. W. Smith et al. 1998), the magnetometers of the FIELDS instrument on PSP (S. D. Bale et al. 2016), and of the Magnetic Field Experiment on board STA (M. H. Acuña et al. 2008); together with solar wind proton moments measured by the Proton and Alpha particle

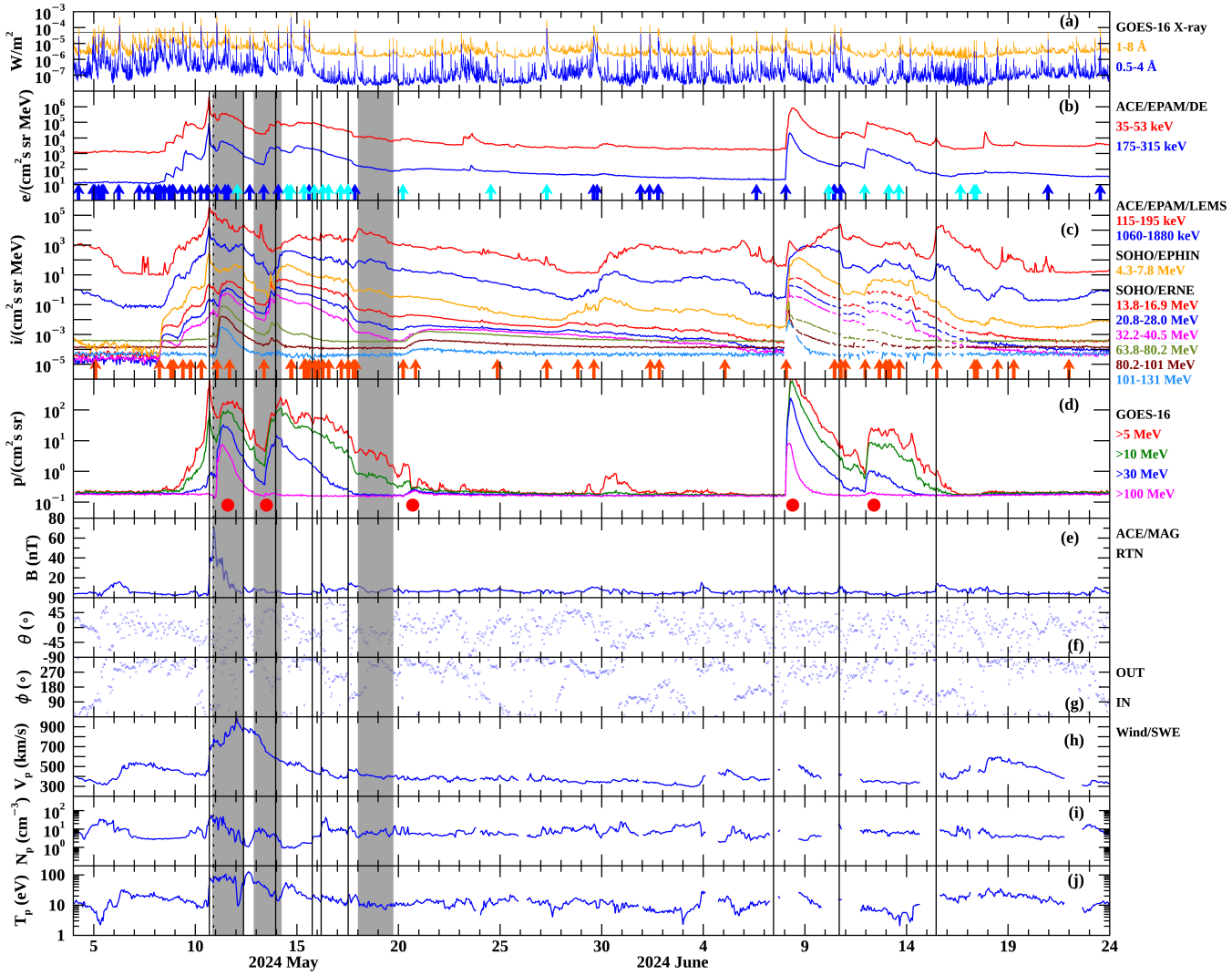

Figure 2. From top to bottom: (a) 1-minute GOES-16 1–8 Å (orange) and 0.5–4 Å (blue) X-ray fluxes; hourly averages of (b) ACE/EPAM/DE electron intensities, (c) ion intensities measured by ACE/EPAM/LEMS120 (blue and red traces), SOHO/EPHIN (orange line), and SOHO/ERNE (six bottom lines), (d) GOES-16 proton integral channels intensities and ACE/MAG magnetic field, (e) magnitude, (f) RTN polar angle, (g) RTN azimuth angle, Wind/SWE solar wind proton, (h) speed, (i) density, and (j) temperature. The thin vertical lines indicate IP shock passages, and the gray-shaded columns ICME passages. The horizontal line in panel (a) indicates the flux level of a GOES M5.0 X-ray class flare. The dark-blue (cyan) arrows in panel (b) indicate the occurrence of >M5.0 X-ray class as observed by GOES-16 (SolO/STIX) as listed in Table 1. The red arrows in panel (c) indicate the occurrence of >800 km s^{-1} CMEs listed in Table 2. The red dots in panel (d) indicate the occurrence of SEP events with >100 MeV proton intensity enhancements.

Sensor (PAS) of the Solar Wind Analyzer on board SolO (C. J. Owen et al. 2020), the Solar Wind Experiment (SWE) on board Wind (K. W. Ogilvie et al. 1995), the Solar Probe Cup of the Solar Wind Electrons Alphas and Protons investigation (J. C. Kasper et al. 2016) on board PSP, and the Plasma and Suprathermal Ion Composition instrument (A. B. Galvin et al. 2008) on board STA.

3. Overview of Energetic Particle Measurements: 2024 May 4–2024 June 24

Figure 2 shows data collected by near-Earth spacecraft from 2024 May 4 to June 24, in particular, from top to bottom, (a) X-ray intensities in two different energy ranges as measured by GOES-16/XRS; (b) electron intensities at two different energies collected by ACE/EPAM/DE; (c) ion intensities measured at two energy channels (top red and blue traces) of ACE/EPAM/LEMS120, and proton intensities measured by SOHO/EPHIN (orange trace) and SOHO/ERNE (six bottom traces at energies >13.8 MeV); (d) proton measurements in four integral channels from GOES-16/SGPS; (e) the interplanetary magnetic field (IMF) magnitude and (f)–(g) IMF angular directions in RTN coordinates as measured by ACE/MAG (ϕ azimuth and θ elevation); and (h)–(j) solar wind proton speed, density, and temperature measured by Wind/SWE. The vertical black lines indicate the passage of IP shocks identified as an abrupt discontinuous increase of the magnetic field magnitude, and the gray-shaded bars indicate the passage of interplanetary CMEs (ICMEs) as reported in the Near-Earth Interplanetary Coronal Mass Ejections (NEICMEs) catalog updated from I. G. Richardson & H. V. Cane (2010).[22]

The horizontal thin line in Figure 2(a) indicates the flux level corresponding to a GOES M5.0 X-ray class flare. The

[22] https://izw1.caltech.edu/ACE/ASC/DATA/level3/icmetable2.html; doi: 10.7910/DVN/C2MHTH.

dark-blue arrows in Figure 2(b) indicate the occurrence of X-ray flares above a class M5.0 as observed by GOES-16. In addition to GOES X-ray observations of Earth-facing flares, STIX on board SolO provided, during this period, observations of flares occurring on the far side of the Sun. The calibration between SolO/STIX 4–10 keV and GOES/XRS 1–8 Å measurements allows the categorization of the STIX flares into the different GOES X-ray classes (see details in H. Xiao et al. 2023; M. Z. Stiefel et al. 2025). The cyan arrows in Figure 2(b) indicate the occurrence of >M5.0 flares observed by STIX using this equivalence between STIX measurements and GOES X-ray flares. Table 1 lists the peak flux times, X-ray flare class, and Stonyhurst coordinates of the flares indicated by arrows in Figure 2(b), along with the ARs in which they originated as reported in the event list of the NOAA Space Weather Prediction Center (SWPC)[23] and the STIX flare list maintained by Laura Hayes.[24]

At the beginning of the period plotted in Figure 2, AR 13663 was the main producer of ⩾ M5 flares, but starting on May 8, AR 13664 became the main producer of ⩾ M5 flares as its magnetic flux and free energy strongly increased (R. Jarolim et al. 2024; H. Hayakawa et al. 2025; I. Kontogiannis et al. 2025). AR 13664 rotated beyond the west limb of the Sun on May 14, when STIX enabled the identification and localization of multiple ⩾ M5 flares throughout the transit of the AR on the far side of the Sun. This AR (renamed as AR 13697) returned to the Earth-facing side of the Sun on May 28 producing further ⩾ M5 flares (Table 1). AR 13685 was another significant region during this period, producing several intense solar flares observed by STIX even before rotating onto the Earth-facing side of the Sun on May 15.

The most intense flare throughout this period was an X16.5 flare with onset at 05:12 UT on 2024 May 20 at Stonyhurst coordinates S19W171 (Carrington longitude, hereafter CL, = 349°). The STIX detector has a built-in attenuator system to protect against large X-ray fluxes. When the count rate exceeds a certain threshold, the 30 imaging detectors and the coarse flat detector of STIX, but not the background (BKG) detector, are covered by a movable aluminum attenuator that prevents detector saturation (S. Krucker et al. 2020). Figure 3 shows the STIX count rates during the X16.5 flare normalized to their respective maxima as measured by the BKG detector in the thermal range (4–10 keV), and by the imaging collimators for the nonthermal range (50–100 keV), which is not affected by the attenuator. Starting at about ∼05:25 UT, the gradual increase in nonthermal counts was due to the arrival of high-energy SEPs interacting with the instrument (see H. Collier et al. 2024). The nonthermal emission at 50–100 keV showed a very impulsive rise with a peak at 05:13 UT, while the thermal emission at 4–10 keV reached its maximum only 1 minute later. Taking the STIX thermal counts as a proxy for the GOES flux, we estimate a GOES rise time of less than 5 minutes. This is significantly shorter than the average rise of ∼13 minutes that has been derived for X-class flares (A. Veronig et al. 2002), which stresses the impulsive nature of this flare. Using calibrated count rates from the BKG detector, M. Z. Stiefel et al. (2025) estimated the class of this flare to be X16.5±1.8. Note that the same calibration is used in Table 1 for assigning X-ray classes to the flares observed by

[23] https://www.swpc.noaa.gov/products/solar-and-geophysical-event-reports
[24] https://github.com/hayesla/stix_flarelist_science/

Table 1
$M \geqslant 5.0$ X-ray Flares between 2024 May 4 and June 23

Peak Time (mm-dd hh:ss) (1)	Class (2)	Lat (deg) (3)	Long (deg) (4)	AR (5)
05-04 06:19	M9.1	N26	W08	13663
05-04 23:48	M9.0	N26	W10	13663
05-05 01:27	M8.4	N26	W10	13663
05-05 06:01	X1.3	N26	W10	13663
05-05 10:00	M7.4	N26	W21	13663
05-05 11:54	X1.2	N26	W22	13663
05-06 06:35	X4.5	N26	W35	13663
05-07 06:16	M5.1	N26	W47	13663
05-07 16:30	M8.2	N25	W56	13663
05-08 01:41	X1.0	N25	W58	13663
05-08 05:09	X1.0	S22	W10	13664
05-08 06:53	M7.1	S21	W18	13664
05-08 12:04	M8.6	S20	W11	13664
05-08 17:53	M7.9	S17	W13	13664
05-08 21:40	X1.0	S20	W17	13664
05-08 22:27	M9.8	S22	W22	13664
05-09 09:13	X2.2	S20	W25	13664
05-09 17:44	X1.1	S18	W29	13664
05-10 06:54	X3.9	S18	W37	13664
05-10 14:11	M5.9	S16	W40	13664
05-11 01:23	X5.8	S17	W47	13664
05-11 11:44	X1.5	S19	W60	13664
05-11 15:25	M8.8	S17	W53	13664
05-12 01:31	M4.6^{STIX}	S12	E137^{STIX}	13685
05-12 16:26	X1.0	S18	W72	13664
05-13 09:44	M6.6	S22	W81	13664
05-14 02:09	X1.7	S19	W89	13664
05-14 12:49	X1.5^{STIX}	S18	W92^{STIX}	13664
05-14 16:47	X11.1^{STIX}	S18	W95^{STIX}	13664
05-15 08:18	X9.7^{STIX}	S18	W104^{STIX}	13664
05-15 08:32	X4.7^{STIX}	S18	W104^{STIX}	13664
05-15 14:38	X2.9	S12	E90	13685
05-15 20:37	X9.5^{STIX}	S18	W112^{STIX}	13664
05-16 06:33	M5.0^{STIX}	S19	W116^{STIX}	13664
05-16 13:25	X3.8^{STIX}	S19	W120^{STIX}	13664
05-17 03:39	M8.0^{STIX}	S18	W130^{STIX}	13664
05-17 12:27	X8.1^{STIX}	S17	W136^{STIX}	13664
05-17 21:08	M7.2	S12	E62	13685
05-20 05:14	X16.5^{STIX}	S19	W171^{STIX}	13664
05-24 12:57	M9.8^{STIX}	S19	E130^{STIX}	13664
05-27 07:08	X2.9^{STIX}	S19	E107^{STIX}	13697
05-29 14:37	X1.4	S21	E66	13697
05-29 18:41	M5.7	N28	E12	13691
05-31 22:03	X1.1	S17	E32	13697
06-01 08:48	X1.4	S17	E27	13697
06-01 18:36	X1.0	S17	E24	13697
06-01 19:39	M7.3	S17	E21	13697
06-06 15:06	M6.1	S20	W41	13697
06-08 01:49	M9.7	S18	W53	13697
06-10 04:10	M6.4^{STIX}	S16	E102^{STIX}	13685 (13713)
06-10 10:58	M5.3	S18	W91	13697
06-10 11:08	X1.5	S19	W92	13697
06-10 18:40	M9.5	S18	W96	13697
06-11 22:38	X2.7^{STIX}	S19	W113^{STIX}	13697
06-13 03:05	X2.5^{STIX}	S19	W128^{STIX}	13697
06-13 14:58	M5.3^{STIX}	S20	W140^{STIX}	13697
06-16 15:38	M9.7^{STIX}	S18	W177^{STIX}	13697
06-17 08:02	M5.8^{STIX}	S22	E165^{STIX}	13697
06-17 10:20	X3.1^{STIX}	S18	E172^{STIX}	13697
06-20 23:16	M5.7	S14	E57	13719
06-23 13:01	M9.3	S17	E74	13723

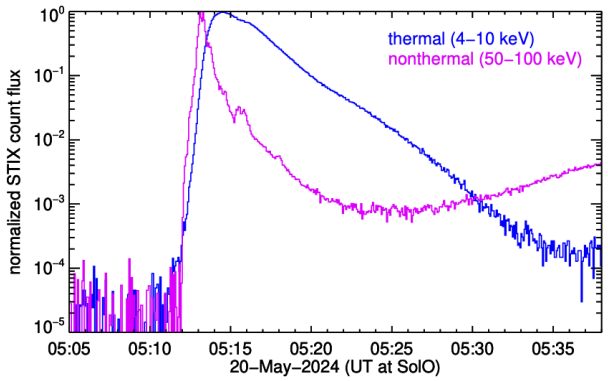

Figure 3. X-ray count rates derived from pixelated STIX science data integrated over two energy ranges. The counts in the thermal range (4–10 keV) are obtained from the BKG detector, since this is not covered by the attenuator (see text for more details). For the nonthermal regime (50–100 keV), all imaging collimators were used since this energy range is not affected by the attenuator. A preevent background has been subtracted, and the count rates have been normalized to their respective maxima. The gradual increase in the nonthermal counts starting at ~05:25 UT is due secondary X-rays produce by high-energy SEPs interacting with the instrument.

STIX. The flare on 2024 May 20 not only was the most intense flare of the period analyzed here but also, at the time of writing, produced the highest nonthermal emission count rate ever recorded by SolO. Note that the largest 4–10 keV peak count rate observed by SolO throughout its mission occurred later at the end of 2024 July 22, during another major flare when SolO was at a distance of 0.92 au.

The red arrows in Figure 2(c) indicate the occurrence of >800 km s^{-1} CME as reported by either the LASCO Coordinated Data Analysis Workshop (CDAW) catalog (S. Yashiro et al. 2004)[25] or the NASA Community Coordinated Modeling Center (CCMC) Space Weather Database Of Notifications, Knowledge, Information (DONKI) system[26] using the real-time analyses performed by the Moon to Mars (M2M) Space Weather Analysis Office (SWAO).[27] M2M/SWAO analysts use the NOAA/SWPC CME Analysis Tool (SWPC/CAT; G. Millward et al. 2013) applied to concurrent coronagraph images from SOHO and STEREO to calculate the size, propagation direction, and speed of either the CME leading edge or the shock front formed ahead of the CME (if observed). In contrast, the CDAW/LASCO catalog uses only SOHO coronagraph images to infer the central position angle (PA) of the CME (defined as the angle measured counterclockwise from the solar north), its angular width, ω_{POS}, as measured in the coronagraph images, and its plane-of-sky speed V_{POS}.

In column (1) of Table 2, we list the time of the first observation of the CME (usually in the LASCO/C2 coronagraph at $R > 2.5\ R_{\odot}$). Columns (2)–(4) of Table 2 provide the propagation direction (longitude and latitude in HEEQ coordinates) and the speed of either the leading edge of the CME (indicated with LE) or the nose of shock front (if observed). Column (5) lists the estimated half-width $\omega_{1/2}$ of the CME or the shock if visible. With the exception of the CME on 2024 June 5 at 01:25 UT, which is based on plane-of-sky estimates, the CME parameters in columns (1)–(5) are based on SWPC/CAT. Considering that throughout this time interval only SOHO and STA coronagraphs were used, and that the longitudinal separation among these two spacecraft ranged from 12°–17°, the CME/shock parameters derived from SWPC/CAT should be judiciously considered. Columns (6)–(8) list PA, ω_{POS} and V_{POS} of the CMEs as listed in the LASCO/CDAW catalog (PA is described as halo when the angular width eventually reaches 360°). Columns (9)–(13) list the peak time, X-ray class, latitude, longitude (in Stonyhurst coordinates), and AR of the solar flare concomitant with the origin of the CME. When no X-ray flare can be associated, but a filament (DSF) or an EUV eruption is observed, this is indicated in Table 2. The association of these solar events with the CMEs is based on examination of SDO/AIA, SolO/EUI/FSI images, STIX flare locations, and NOAA/SWPC solar event lists,[28] inspection of timing, solar event locations, CME propagation directions, as well as a comparison with the associations made in the CCMC/DONKI database. Note that the X-ray classes assigned to the flares observed by STIX have been obtained using the calibrated count rates from the BKG detector (except for the flare peaking at 10:09 UT on May 15 when no pixelated BKG data were available).

In terms of SEPs (Figures 2(b)–(d)), the effects of AR 13664 at Earth started to become visible on May 8, with a sequence of electron and low-energy ($\lesssim$40 MeV) proton intensity enhancements that peaked with the arrival of an IP shock on May 10 at 16:36 UT. This shock marked the onset of plasma compressions affecting Earth's magnetosphere that, combined with a sequence of ICMEs, caused the great geomagnetic storms of 2024 May (e.g., Y.-S. Kwak et al. 2024; H. Hayakawa et al. 2025). The gray-shaded vertical bars in Figure 2 indicate ICME passages as identified in the NEICMEs catalog. A more detailed identification of individual ICMEs, their solar origins, and possible interactions is discussed elsewhere (e.g., S. Khuntia et al. 2025).

The period shown in Figure 2 was marked by elevated low-energy ($\lesssim$13 MeV) proton intensities as observed by SOHO/ERNE for at least 7 weeks starting on May 8 (Figure 2(c)). By contrast, at higher energies, only five >100 MeV proton intensity enhancements were observed (bottom blue line in Figure 2(c) and purple line in Figure 2(d)). These >100 MeV proton increases are indicated by red dots in Figure 2(d). The first one occurred early on May 11 after the passage of the shock on May 10. This SEP event was observed by neutron monitor stations and designated as GLE-74. The solar origin of GLE-74 was associated with a ~1800 km s^{-1} CME and an X5.8 flare from AR 13664 at S17W47 (see details in A. Papaioannou et al. 2025). A second >100 MeV proton intensity enhancement occurred on May 13 associated with a ~1900 km s^{-1} CME and an M6.6 flare from the same AR then at S22W81 (e.g., L. Rodríguez-García et al. 2025). The third >100 MeV proton intensity increase occurred on May 20 and is analyzed below in Section 4. This event led to a period of elevated >80 MeV proton intensity observed by SOHO/ERNE that lasted about ~2 weeks.

With the return of AR 13664 to the Earth-facing side of the Sun (renamed AR 13697), two additional >100 MeV proton events were observed. The first was early on June 8 (GLE-75), associated with a ~1500 km s^{-1} CME and an M9.8 flare from S17W68 (S. Poluianov et al. 2025). The second, with the onset

[25] https://cdaw.gsfc.nasa.gov/CME_list/
[26] https://ccmc.gsfc.nasa.gov/tools/DONKI/
[27] https://science.gsfc.nasa.gov/674/m2m-website.html
[28] https://www.swpc.noaa.gov/products/solar-and-geophysical-event-reports

Table 2
Prior >800 km^{-1} CMEs and $M > 5.0$ X-Ray Flares

C2 Start Time (yyyy-mm-dd hh:ss) (1)	Long[a] (deg) (2)	Lat[a] (deg) (3)	V_{CME}[a] (km s^{-1}) (4)	$\omega_{1/2}$[a] (deg) (5)	PA (deg) (6)	ω_{POS} (deg) (7)	V_{POS} (km s^{-1}) (8)	Peak Time (mm-dd hh:ss) (9)	Class (10)	Lat (deg) (11)	Long (deg) (12)	AR (13)
2024-05-04 06:53	−02	29	804	23	12	205	576	05-04 06:19	M9.1	N26	W09	13663
2024-05-08 05:36	09	−07	870	43^{LE}	Halo	360	530	05-08 05:09	X1.0	S22	W10	13664
2024-05-08 12:24	08	−15	1156	43	Halo	360	677	05-08 12:04	M8.6	S20	W11	13664
2024-05-08 19:12	−23	03	828	38^{LE}	82	141	401	05-08 15:50	DSF	N12	E12	⋯
2024-05-08 22:24	05	−06	1257	45	Halo	360	952	05-08 21:40	X1.0	S20	W17	13664
2024-05-09 09:24	14	−12	1561	45	Halo	360	1280	05-09 09:13	X2.2	S20	W25	13664
2024-05-09 18:23	12	−05	1236	45	Halo	360	1024	05-09 17:44	X1.1	S18	W29	13664
2024-05-10 07:12	15	−10	1332	45	Halo	360	953	05-10 06:54	X3.9	S18	W37	13664
2024-05-11 01:36	15	−02	1820	48	Halo	360	1614	05-11 01:23	X5.8	S17	W47	13664
2024-05-11 03:12	50	05	1032	38^{LE}	⋯	⋯	⋯	⋯	⋯	⋯	⋯	⋯
2024-05-11 16:24	53	−02	946	25^{LE}	268	93	846	05-11 15:25	M8.8	S17	W53	13664
2024-05-13 08:48	26	−12	1935	50	Halo	360	1690	05-13 09:44	M6.6	S22	W81	13664
2024-05-14 02:00	95	00	502	34^{LE}	274	172	805	05-14 02:09	X1.7	S19	W89	13664
2024-05-14 17:00	134	14	2225	42	Halo	360	2010	05-14 16:47	X11.1^{STIX}	S18	W95^{STIX}	13664
2024-05-14 17:30	96	02	1199	38^{LE}	⋯	⋯	⋯	⋯	⋯	⋯	⋯	⋯
2024-05-14 17:48	−72	16	1292	43^{LE}	Halo	360	1407	05-14 17:38	M4.4	N18	E72	13682
2024-05-15 08:36	105	02	1766	31^{LE}	Halo	360	1648	05-15 08:18	X9.7^{STIX}	S18	W104^{STIX}	13664
2024-05-15 08:48	114	−29	1082	24^{LE}	⋯	⋯	⋯	05-15 08:32	X4.7^{STIX}	S18	W104^{STIX}	13664
2024-05-15 10:00	113	−06	1205	37^{LE}	⋯	⋯	⋯	05-15 10:09	M2.7^{STIX}[b]	S25	W97^{STIX}	13664
2024-05-15 10:36	−13	46	805	31^{LE}	356	86	556	05-15 09:15	loop eruption	N35	E35	⋯
2024-05-15 10:48	109	−16	1162	39^{LE}	254	114	993	⋯	⋯	⋯	⋯	⋯
2024-05-15 14:53	−92	−17	1570	42^{LE}	⋯	⋯	⋯	05-15 14:38	X2.9	S12	E90	13685
2024-05-15 16:30	⋯	⋯	⋯	⋯	138	190	1570$^{only\ C3}$	⋯	⋯	⋯	⋯	⋯
2024-05-15 20:56	110	02	1269	29^{LE}	Halo	360	1250	05-15 20:37	X9.5^{STIX}	S18	W112^{STIX}	13664
2024-05-16 01:25	105	00	1103	22^{LE}	268	38	1000	05-16 01:18	M2.1^{STIX}	S19	W114^{STIX}	13664
2024-05-16 06:48	109	−01	1110	21^{LE}	264	37	881	05-16 06:33	M5.0^{STIX}	S19	W116^{STIX}	13664
2024-05-16 08:12	−70	−05	1298	17^{LE}	87	49	1216	05-16 08:04	M1.0	S10	E85	13685
2024-05-16 13:36	120	−02	1452	27^{LE}	260	258	1102	05-16 13:25	X3.8^{STIX}	S19	W120^{STIX}	13664
2024-05-17 04:28	−20	−01	854	10^{LE}	⋯	⋯	⋯	05-17 04:02	DSF	S08	E20	13679
2024-05-17 12:48	155	04	1625	50	Halo	360	1160	05-17 12:27	X8.1^{STIX}	S17	W136^{STIX}	13664
2024-05-17 18:48	110	−20	942	24^{LE}	248	43	714	⋯	⋯	⋯	⋯	⋯
2024-05-17 20:48	−65	−13	1129	37^{LE}	92	260	1098	05-17 21:08	M7.2	S12	E62	13685
2024-05-20 05:36	172	02	2678	45	Halo	360	1459	05-20 05:14	X16.5^{STIX}	S19	W171^{STIX}	13664
2024-05-20 19:36	−38	−06	836	17^{LE}	100	67	609	05-20 19:51	C4.6	S20	E35	13685
2024-05-23 22:36	−80	−05	943	15^{LE}	91	32	958	05-23 22:18	EUV eruption	N19	E80	13690
2024-05-24 20:48	90	04	854	18^{LE}	274	73	699	05-24 20:25	M1.4	S05	W89	13679
2024-05-27 07:23	−133	−02	1254	50	Halo	360	1291	05-27 07:08	X2.9^{STIX}	S19	E107^{STIX}	13664 (13697)
2024-05-28 19:48	141	−56	976	28^{LE}	208	60	789	05-28 19:27	C6.6^{STIX}	S24	W164^{STIX}	13679
2024-05-29 01:48	161	31	853	32^{LE}	Halo	360	518	05-29 01:08	M1.1^{STIX}	S10	W157^{STIX}	13679
2024-05-29 14:48	−129	01	1033	45	Halo	360	823	05-29 14:37	X1.4	S23	E70	13697
2024-05-31 03:47	−171	−61	817	21^{LE}	197	44	631	05-31 03:22	C3.1^{STIX}	S25	E164	⋯
2024-06-01 18:48	−168	−06	1503	45	Halo	360	946	06-01 18:45	M3.1^{STIX}	S10	E167	13679
2024-06-01 20:00	−24	−14	898	27^{LE}	⋯	⋯	⋯	06-01 19:39	M7.3	S20	E21	13697
2024-06-05 01:25	−^{PoS}	−06	1051	19^{LE}	96	136	1193	06-05 01:03	C3.3^{STIX}	S09	E121	13713?
2024-06-08 01:53	24	−03	1528	45	Halo	360	1638	06-08 01:52	M9.8	S17	W53	13697
2024-06-10 10:48	91	07	983	37^{LE}	284	246	972	06-10 10:58	M5.3	S18	W91	13697

Table 2
(Continued)

C2 Start Time (yyyy-mm-dd hh:ss) (1)	Long[a] (deg) (2)	Lat[a] (deg) (3)	V_{CME}[a] (km s^{-1}) (4)	$\omega_{1/2}$[a] (deg) (5)	PA (deg) (6)	ω_{POS} (deg) (7)	V_{POS} (km s^{-1}) (8)	Peak Time (mm-dd hh:ss) (9)	Class (10)	Lat (deg) (11)	Long (deg) (12)	AR (13)
2024-06-10 11:12	119	18	1117	48	…	…	…	06-10 11:08	X1.5	S18	W92	13697
2024-06-10 18:36	139	03	1352	48	290	249	1240	06-10 18:40	M9.5	S18	W96	13697
2024-06-10 23:36	138	−41	914	38^{LE}	208	181	697	06-10 22:30	prominence eruption	S35	∼W105	…
2024-06-11 23:06	113	26	1312	48^{LE}	Halo	360	1988	06-11 22:38	X2.7^{STIX}	S19	W113	13697
2024-06-12 16:00	125	−07	862	35^{LE}	271	218	727	06-12 15:10	M2.1^{STIX}	S19	W112	13697
2024-06-12 23:24	−171	−06	1357	45^{LE}	Halo	360	751	…	…	…	…	…
2024-06-13 03:48	126	13	1037	21^{LE}	302	126	729	06-13 03:00	M1.7^{STIX}	S19	W128	13697
2024-06-13 04:53	138	11	1187	24^{LE}	…	…	…	06-13 03:05	X2.5^{STIX}	S19	W128	13697
2024-06-13 15:24	148	07	1037	45^{LE}	273	183	602	06-13 14:49	M5.3^{STIX}	S18	W138	13697
2024-06-15 11:48	−09	−66	812	29^{LE}	165	113	689	06-15 11:17	DSF	S40	E20	…
2024-06-17 08:24	−151	−34	902	39^{LE}	Halo	360	691	06-17 08:02	M5.8^{STIX}	S22	E165	13697
2024-06-17 11:24	144	24	974	31^{LE}	Halo	360	448	06-17 10:20	X3.1^{STIX}	S18	E172	13697
2024-06-19 06:48	75	−05	1111	20^{LE}	249	107	893	06-19 06:38	M1.1	S12	W79	13711
2024-06-21 23:48	−121	−01	1208	52	66	268	1183	06-21 23:43	M4.0^{STIX}	S16	E104	13697

Notes.
[a] DONKI/CCMC parameters of the shock front when identifiable (otherwise of the CME leading edge indicated by LE).
[b] X-ray class equivalent computed using quick-look STIX intensity-time, since BKG data were unavailable.

late on June 11, was associated with a $\gtrsim$1300 km s^{-1} CME and an X2.7 flare from AR 13697 behind the west limb of the Sun as seen from Earth. In contrast to the first frontside passage of AR 13664 (April 30–May 14) when several fast CMEs were Earth directed (e.g., S. Khuntia et al. 2025), only the flanks of IP shocks without ICMEs impacted Earth well after AR 13697 had returned to the visible side of the Sun on May 28. The production of intense SEP events was more sporadic, and high-energy SEP events were observed near Earth only after AR 13697 was on the west side of the Sun.

Owing to the longitudinal separation among the different spacecraft (Figure 1), the energetic particle intensity-time profiles at PSP and SolO throughout the period under study differ significantly from those at STA and SOHO. Figure 4 shows proton intensities at energies above ~20 MeV observed by SOHO/ERNE (green), STA/HET (red), the sunward-looking aperture A of the High-Energy Telescope of the EPI-Hi instrument on board PSP (EPI-Hi/HETA; purple), and the sunward-looking aperture of the EPD High-Energy Telescope on SolO (EPD/HET-SUN; blue). Each panel shows proton intensities at similar energy channels collected by these instruments without applying any rescaling factor or removal of instrumental background intensities. In contrast to SOHO/ERNE, the EPI-Hi/HETA and EPD/HET-SUN proton intensities in the plotted energy channels are essentially free of a significant instrumental background; however, because of their smaller geometric factors, the intensities required to trigger count rates in the PSP and SolO instruments are generally higher than in SOHO/ERNE. Similarly, STA/HET also provides a clean background (except for the 40–60 and 60–100 MeV energy channels), but its larger geometric factor allows measurements at lower intensities than at EPD/HET-SUN and EPI-Hi/HETA. We note that PSP performed a number of spacecraft maneuvers (or rolls) during the plotted period. We verified that these spacecraft rolls did not have any apparent effects on the intensities shown in Figure 4. Additionally, particle intensities during this period occasionally triggered the EPI-Hi dynamic thresholds (see details in C. M. S. Cohen et al. 2021). Notably, during the entire SEP event on May 20 (analyzed in detail in Section 4 and indicated by the shaded orange area in Figure 4), the EPI-Hi instruments (both LET and HET) stayed in their nominal dynamic threshold mode (DT-0). Starting on May 31, PSP started performing high-speed data transfers to Earth, which required powering off onboard instruments, and thus, continuous PSP data were not available after that date.

Because of their close proximity, the intensity-time profiles at STA and SOHO shown in Figure 4 are very similar. PSP intensity enhancements at the energies plotted in Figure 4 began to be observed early on May 11. These small intensity enhancements were followed by large intensity increases that, based on their occurrence timing, intensity-time profile, and parent solar activity location, we associate with (1) the ~1900 km s^{-1} CME and M6.6 flare from AR 13664 at S22W81 peaking at 09:44 UT on May 13 (L. Rodríguez-García et al. 2025), (2) the $\gtrsim$2000 km s^{-1} CME and X11.1 solar flare from AR 13664 at S18W95 peaking at 16:47 UT on May 14, (3) the $\gtrsim$1700 km s^{-1} CME and X9.7 solar flare from AR 13664 at S18W104 peaking at 08:18 UT on May 15, and (4) the ~1600 km s^{-1} and X8.1 solar flare from AR 13664 at S17W136 peaking at 12:27 UT on May 17 (see Table 2 for details of these CMEs and flares). Several transient solar wind structures, such as IP shocks and ICMEs, affected the SEP intensity-time profiles at PSP throughout the period May 11–18. The list of such IP shocks and ICMEs at PSP can be found in the Helio4cast catalog (C. Möstl et al. 2017, 2020).[29] These structures most likely originated in the sequence of CMEs erupting from AR 13664 as it transited over the west limb of the Sun (see Table 2).

At SolO, >20 MeV proton intensity enhancements were observed early on May 12. Based on their occurrence timing, location, and intensity-time profile, we associate the origin of the high-energy particle intensity increases with prominent solar events as follows. The first particle counts were probably related to the M4.6 flare seen by STIX from AR 13685 at S12E137 (Table 1). This first small intensity enhancement was followed by a clear intensity increase most likely associated with the ~1900 km s^{-1} CME and an M6.6 flare from AR 13664 at S22W81 (L. Rodríguez-García et al. 2025). In contrast to SOHO/ERNE where >100 MeV protons were detected, at SolO, protons were only detected at energies $\lesssim$53 MeV. A new >20 MeV proton intensity enhancement occurred in the second half of May 14, probably associated with the $\gtrsim$2000 km s^{-1} CME and X11.1 flare from AR 13664 at S18W95 (Table 2), although the elevated preevent intensities hinder precise determination of the SEP event onset. A new enhancement, most likely associated with the ~1500 km s^{-1} CME and X2.9 flare from AR 13685 at S12E90 peaking at 14:38 UT on May 15, was observed even at $\gtrsim$70 MeV protons, although contributions from CMEs originating from AR 13664 early on May 15 cannot be discarded.

After May 17, with no relevant SEP injections observed for more than ~2 days, proton intensities at all four spacecraft gradually decreased with comparable levels, indicating the formation of an energetic particle reservoir spanning at least ~170° in longitude. This period was interrupted by a new SEP injection on May 20 temporally associated with the X16.5 flare from AR 13664 at S19W171 (Figure 3). Notably, this flare occurred after 2 days of relatively low solar activity (I. Kontogiannis et al. 2025). This SEP injection constituted the most intense SEP event throughout the period plotted in Figure 4 as observed by PSP and SolO. By contrast, both STA and SOHO detected a gradual increase that developed into a long-lasting period of elevated particle intensities extending until about June 7. Throughout the decay phase of this SEP event, comparable proton intensities were observed at the four spacecraft, only briefly interrupted by some injections at PSP most likely associated with a ~900 km s^{-1} CME on May 28, and at SolO most likely associated with CMEs early on May 27 from AR 13697 and in the second half of June 1 from AR 13679 (Table 2). The following section provides a detailed analysis of the solar origin and properties of the intense SEP event on 2024 May 20 as observed by the different spacecraft.

4. The 2024 May 20 SEP Event

In this section, we discuss the main details of the SEP event on 2024 May 20 (henceforth the M20 SEP event). We pay special attention to its solar origin, the IP context where the event occurred, the main properties of the SEP event as observed by the different spacecraft, and how these properties depend on the magnetic connectivity of the spacecraft to the presumed particle sources. Apart from its large intensities at

[29] https://helioforecast.space/icmecat; doi: 10.6084/m9.figshare.6356420.

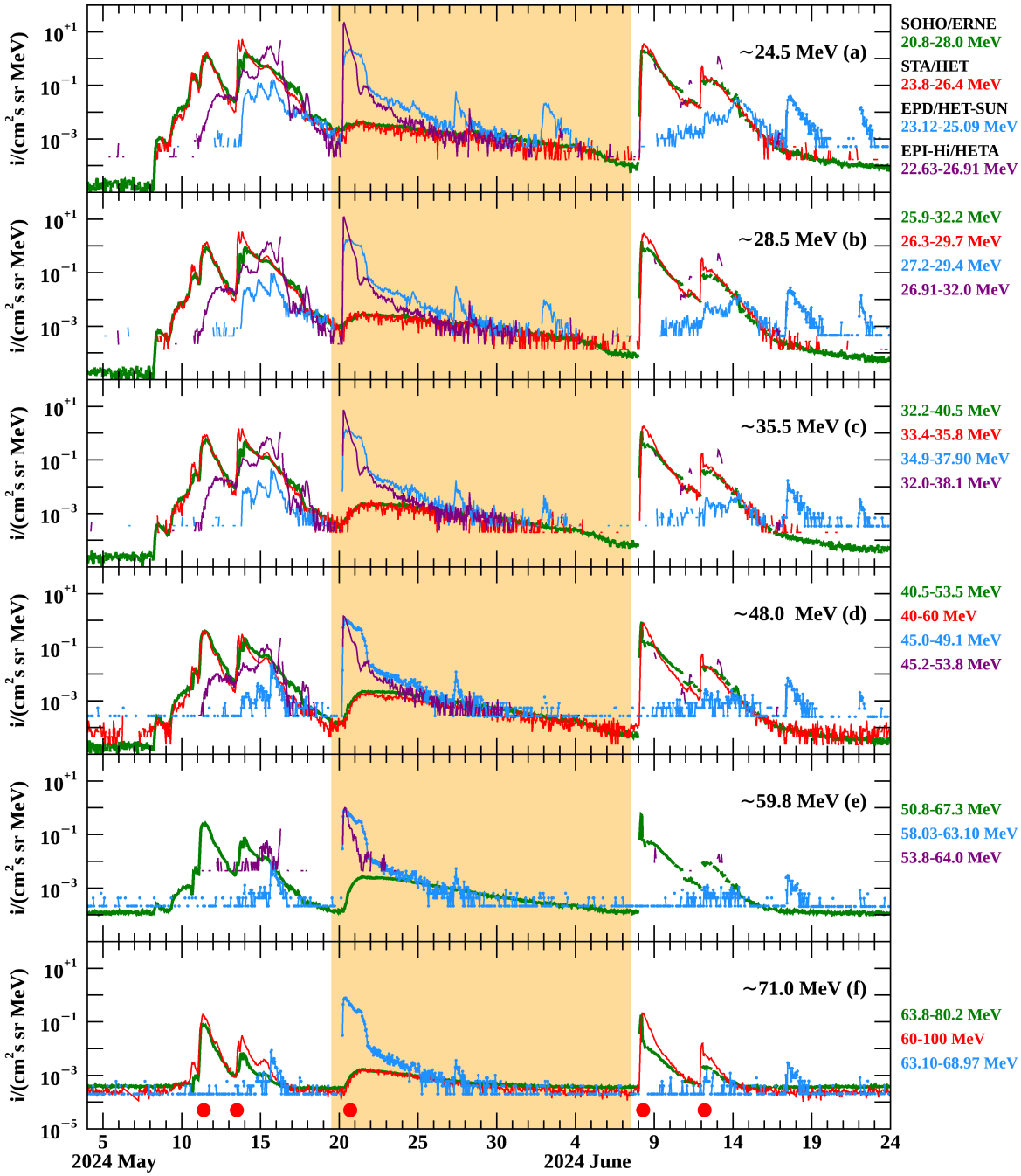

Figure 4. 1 minute averages of the proton intensities measured by SolO/EPD/HET-SUN (blue), PSP/EPI-Hi/HETA (purple), STA/HET (red), and SOHO/ERNE (green). Each panel shows intensities at similar energy ranges. The shaded orange area highlights the event on 2024 May 20 that resulted in a long-lasting ($\gtrsim$2 week) energetic particle reservoir. The red dots in the bottom panel indicate the occurrence of SEP events at L1 displaying >100 MeV proton intensity enhancements.

PSP and SolO, the M20 SEP event constituted, at the time of writing, the largest event ever recorded on Mars by the Radiation Assessment Detector (RAD) on the Mars Science Laboratory (MSL; D. M. Hassler et al. 2012) as reported by A. Posner et al. (2025). It was also observed in neutron measurements by the Dynamic Albedo of Neutrons (DAN) on board MSL and the High-Energy Neutron Detector on board the Mars Odyssey spacecraft as described by I. Mitrofanov et al. (2025). The detection of >100 MeV protons at L1 during this event and the formation of the long-lasting period of elevated particle intensities at all spacecraft will be analyzed in Section 5.

4.1. Solar Origin

SolO/EUI/FSI images (collected during this period with a cadence of 10 minutes starting on the hour) allowed the EUV observation of the far side of the Sun. The top row of Figure 5 shows a sequence of base-difference images taken by SolO/EUI/FSI at 174 Å, using the image at 05:10 UT as base. An EUV brightening from AR 13664 was observed peaking at the image taken at 05:20 UT. The orange star in Figure 5 indicates the site of this EUV brightening, which coincides with the location of the X16.5 flare as identified in STIX observations,

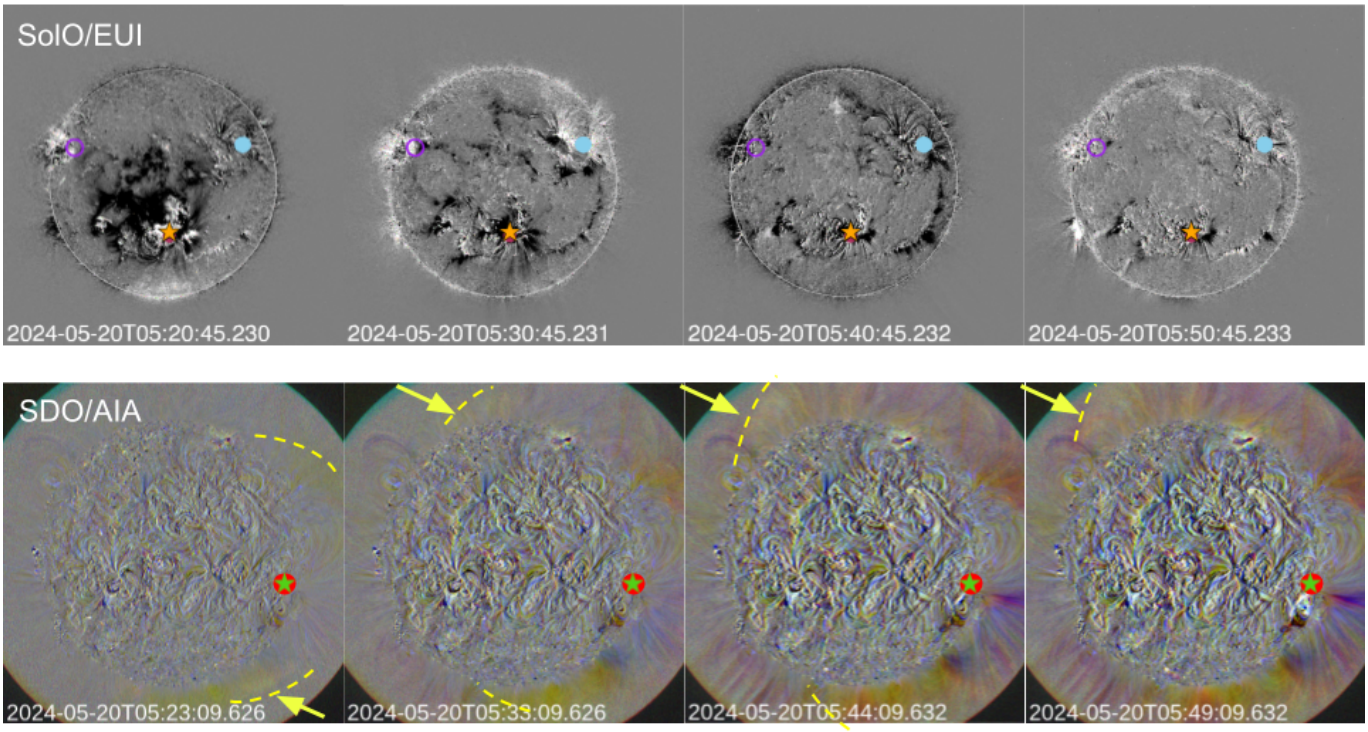

Figure 5. Top row: sequence of SolO/EUI/FSI 174 Å base-difference images (the preeruption image at 05:10 UT was subtracted from all subsequent frames). The orange star indicates the site of the X16.5 flare associated with the origin of the M20 SEP event. The purple open circle (light-blue symbol) indicates the footpoint of the magnetic field line connecting to PSP (SolO) using the method Parker-PFSS described in Section 4.2. Bottom row: sequence of SDO/AIA three-color ratio images combining the wavelengths 211, 193, 171 Å. The red circle (green star) indicates the footpoint of the field line connected to STA (Earth), using the methods described in Section 4.2. Yellow-dashed lines and arrows indicate the over-the-limb EUV signatures in the low corona of the far-side CME associated with the M20 SEP event.

i.e., S19W171. The purple open circle and the light-blue symbol indicate the footpoints of the IMF lines connecting to PSP and SolO, respectively, using the methods to be described in Section 4.2. At 05:20 UT, a darkening region extending northward of the EUV brightening is visible in the top left panel of Figure 5, suggesting that at that time (i.e., 8 minutes after the onset of the X-ray flare) the effects of the solar eruption spanned over an extended region of the solar disk, predominantly toward the east as seen from SolO. Owing to the limited 10 minute cadence, the propagation of the EUV perturbation cannot be clearly discerned as a distinct propagating bright front. However, the darkened patches in the top row of Figure 5 are likely indirect evidence of the passage of the EUV perturbation as it interacts with coronal structures (e.g., R.-Y. Kwon et al. 2013). While these patches do not represent the actual location of the propagating front of the EUV perturbation, we see that, by 05:30 UT, signatures of the EUV perturbation had reached the estimated magnetic footpoints of PSP and SolO. The EUV perturbation seems to reach only a bounded area limited by the dark-black arcs in the second and third top panels of Figure 5, although it is difficult to determine the exact extent of the EUV perturbation over the solar disk as seen from SolO/EUI images. Given the 10 minute cadence of the SolO/EUI/FSI images, a rough estimate of the speed at which this EUV perturbation propagated above the solar disk can be estimated to be about $\sim$300 km s^{-1}.

In contrast to the far-side SolO/EUI/FSI observations, SDO/AIA allows us to study whether the EUV perturbation extended to the Earth-facing side of the Sun. The bottom row of Figure 5 shows three-color ratio images from SDO/AIA. A preevent image was used to estimate the individual ratio images at the three channels used (i.e., 211, 193, and 171 Å) that were then combined into a single frame at each timestamp. This was done with a 1 minute cadence, but only selected frames are shown in Figure 5. The red circle and green star indicate the footpoints of the IMF lines connecting to STA and L1, respectively, using the methods to be described in Section 4.2. The first indication of an eruption from the far side of the Sun is the ejected material that appeared in SDO/AIA images at 05:16 UT over the south limb. By 05:20 UT, these backside over-the-limb EUV signatures had extended over the northwest limb of the Sun as seen from SDO. Yellow-dashed lines and arrows in the bottom panels of Figure 5 indicate the location of this backside material above the solar limb. This backside EUV signal eventually extended above the entire solar limb, forming a halo by $\sim$05:40 UT. Some of these signatures can also be seen above the east limb in the SolO/EUI/FSI image at 05:40 UT (third top panel of Figure 5). However, there is no clear evidence that the EUV perturbation associated with the X16.5 flare propagated over the Earth-facing side of the solar disk.

In order to analyze the longitudinal extent of the SEP event associated with this far-side solar eruption, we considered the possibility that another frontside eruption around the time of the X16.5 flare could have contributed to the observed SEP population observed at L1 and STA. Throughout this period, the most obvious signature of an EUV eruption on the Earth-facing side of the solar disk was an EUV brightening appearing on the southwest as observed from SDO, and on the southeast as observed from SolO, as shown in the fourth

top and bottom panels of Figure 5. This brightening can be associated with a short-duration GOES-16 C6.7 flare from AR 13683 at ∼S20W66 with onset at 05:42 UT, peak at 05:54 UT, and end at 06:16 UT. The EUV signatures of this eruption extended in a narrow range of longitudes toward the south, reaching ∼S50° at about 06:30 UT, but no extension of this eruption could be observed above the solar limb in the EUV images from SDO/AIA, STA/EUVI, or SolO/EUI/FSI. Therefore, establishing a link between this EUV brightening and a CME structure in the WL coronagraph images is difficult. The only possible WL feature that might be associated with this EUV brightening is a structure appearing in the LASCO/C2 field of view at 05:48 UT at PA ∼ 210°, superposed on the large backside halo CME related to the X16.5 flare. This structure can be discerned only in direct LASCO images, but not in running-difference images (see Figure 6). Indeed, neither the CDAW/LASCO nor the DONKI/CME catalogs identified this structure as a new CME. As seen in the LASCO/C2 direct images, this WL feature propagated southwestward (PA ∼ 200°–230°) with the leading edge at PA ∼ 210°, a plane-of-sky speed of V_{POS} ∼ 678 km s^{-1}, and a width ω_{POS} ∼ 30°. Such slow and narrow CMEs are not typically associated with high-energy (≳100 MeV) SEP events (e.g., S. W. Kahler & D. V. Reames 2003; B. Swalwell et al. 2017). Although it could have contributed to the SEP intensity enhancement observed at L1 and STA, its production of high-energy particles and participation into the long-lasting period with >80 MeV proton intensities at L1 are arguable. We note also a very small-scale activity occurring at ∼N60W50 in a weak magnetic field area (PA ∼ 330° in the right three panels in the bottom row of Figure 5). Whereas it is possible that this EUV signature was a response to the far-side CME eruption and wave propagation, there is no evident release of material from this region to higher altitudes nor any motion of any disturbance beyond the spot displayed in Figure 5. Therefore, this EUV signature could barely contribute to the production of SEPs at high energies.

Figure 6 shows the CME associated with the far-side eruption as seen by the WL coronagraphs on board SOHO and STA. Specifically, the first two columns of Figure 6 show running-difference images from LASCO/C2 (Figure 6(a)), LASCO/C3 (Figures 6(d) and (g)), and STA/COR2 (Figures 6(b), (e), and (h)). In order to estimate the 3D structure of the shock driven by this CME, we applied the ellipsoid model developed by R.-Y. Kwon et al. (2014; see also R.-Y. Kwon & A. Vourlidas 2017), which is a forward-modeling approach combining images (as cotemporal as possible) from the different coronagraphs. The assumed geometric shape, i.e., an ellipsoid for the shock front formed ahead of the CME, is projected onto the coronagraph images taking into account the viewing perspectives, and is adjusted until a satisfactory fit is achieved for all viewpoints simultaneously. In the first two columns of Figure 6, we overplot, on top of the SOHO/LASCO (left column) and STA/COR2 (middle column) images, the ellipsoid that best represents the outermost front ahead of the CME. The red-, orange-, blue-, and cyan-dashed lines indicate each quadrant of the ellipsoid, whereas the white-dashed lines outline the whole 3D structure propagating away from Earth (i.e., into the plane of the image). Representing the shock as an ellipsoid is an approximation of its actual shape, especially in this case where the CME displayed some asymmetries and substructures. Furthermore, only two viewpoints (STA and SOHO) separated by just ∼13° in heliolongitude (Figure 1) were used. The reduced cadence of images from the Metis coronagraph on board SolO (E. Antonucci et al. 2020) at that time prevented obtaining a third perspective on this fast CME. The resulting fit yields an ellipsoid with its apex propagating in the direction S02W164 at an estimated speed of ∼2500 km s^{-1} initially at ∼10 $R_\odot$ and gradually reduced to 1500 km s^{-1} at ∼25 $R_\odot$. Note that the CDAW/LASCO catalog estimated a plane-of-sky speed V_{POS} = 1459 km s^{-1} at PA = 264°, whereas the DONKI catalog reported a speed of 2678 km s^{-1} in the direction S02W172 when applying SWPC/CAT to the shock signatures or 1927 km s^{-1} in the direction S00W176 when using the leading edge of the CME. The right column of Figure 6 will be described later in Section 5.1 when discussing the origin of the SEPs observed at STA and L1.

4.2. Magnetic Connection

In order to estimate the region where a spacecraft establishes magnetic connection with the Sun or an IP shock, a series of approximations and assumptions regarding the topology of the magnetic field in both the corona and IP space are required. Among the different methods used in the literature to compute the spacecraft magnetic connectivity with the Sun (e.g., P. MacNeice et al. 2011; D. Lario et al. 2017a; A. P. Rouillard et al. 2020; D. E. da Silva et al. 2023; and references therein), here, we apply the following: (1) Assume a simple ballistic extrapolation of nominal Parker spiral IMF lines from a spacecraft directly to the Sun using the solar wind speed measured at the onset of the SEP event (we designate this method as Parker). (2) Assume a nominal Parker spiral from the spacecraft down to 2.5 $R_\odot$, and then, use the potential field source surface (PFSS) model (e.g., C. J. Schrijver & A. M. Title 2003) applied to the line-of-sight magnetogram data taken by the Helioseismic and Magnetic Imager (P. H. Scherrer et al. 2012) on board SDO to trace the magnetic field lines from 2.5 $R_\odot$ down to the solar surface (we designate this method as Parker+PFSS). (3) Assume a nominal Parker spiral from the spacecraft down to 2.0 $R_\odot$, and then, use the magnetogram built using the Air Force Data Assimilative Photospheric Flux Transport (ADAPT; C. N. Arge et al. 2010) as provided by the magnetic connectivity tool[30] (A. P. Rouillard et al. 2020). Different realizations, assuming slight variations in flux transport parameters, were considered in ADAPT, with #7 as the one selected for this specific case (we designate this method as IRAP-ADAPT). (4) Assume a nominal Parker spiral from the point of observation down to 5 $R_\odot$, and use the Wang–Sheeley–Arge (WSA; C. N. Arge et al. 2004) model, which uses the Schatten current sheet model (K. H. Schatten 1971, 1972) to extend the PFSS solution to 5 $R_\odot$, and then, trace the field lines from 5 $R_\odot$ to the solar surface. Unlike the Parker +PFSS and the IRAP+ADAPT methods, this fourth method (designated as ADAPT/WSA) uses as input a combination of the National Solar Observatory Global Oscillation Network Group (GONG; J. W. Harvey et al. 1996) magnetograms for the Earth-facing side of the Sun and PHI observations from SolO for the far side of the Sun, following the technique described in S. Schonfeld et al. (2024).

[30] Available at https://connect-tool.irap.omp.eu/.

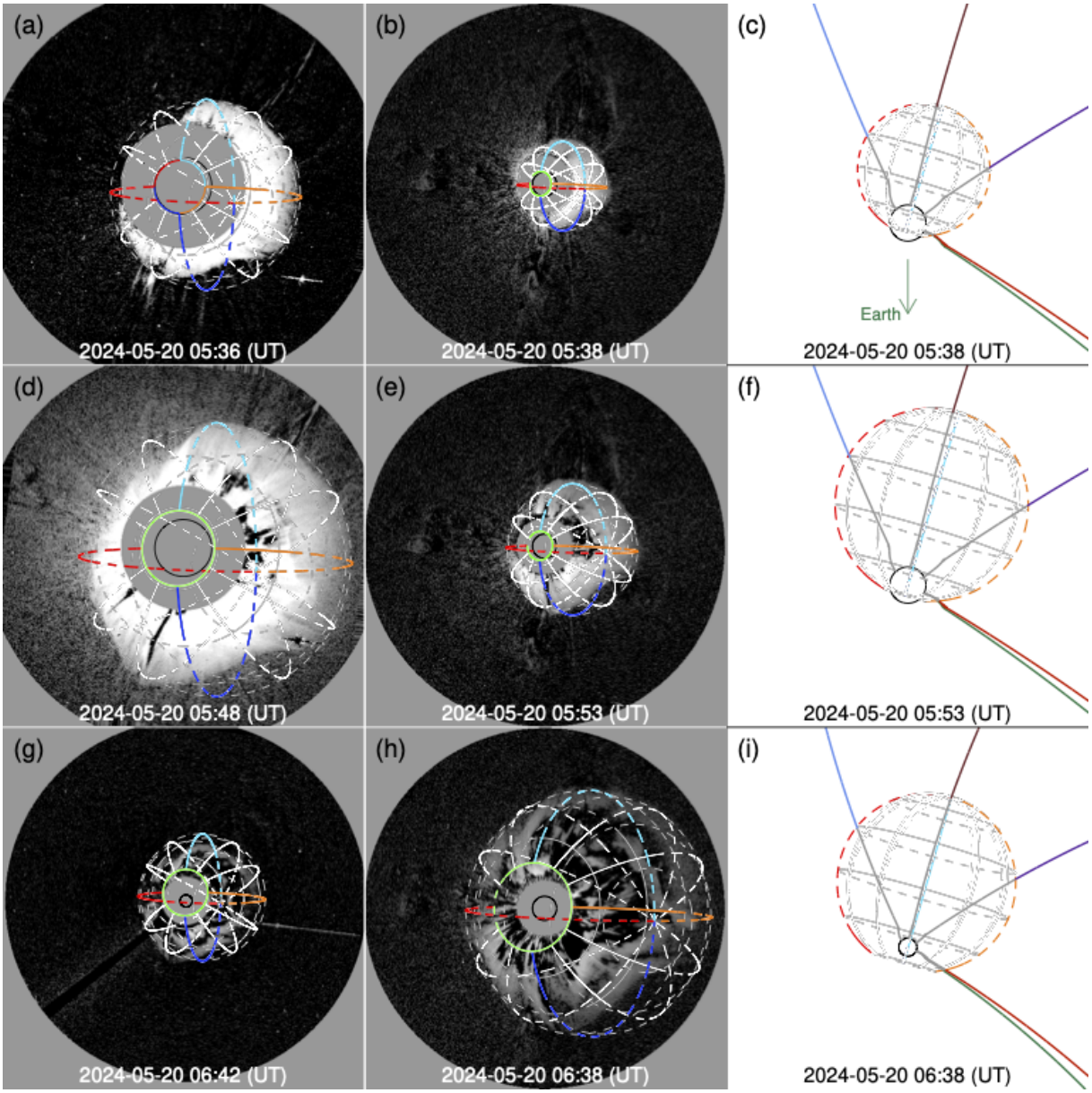

Figure 6. First two columns: selected time series observations of the CME on 2024 May 20 as seen by SOHO/LASCO C2 (two top-left panels) and C3 (bottom left panel), and by STA/COR2 (middle column). The solar center is located at the center of each panel, and the solar rotational axis is the north of each image. The thin black circle in each panel indicates the solar disk. Representations of the reconstructed 3D shock front are shown by white lines outlining the overall structure, with the red, orange, blue, and cyan lines highlighting the four distinct quadrants of the ellipsoid. The solid lines represent the portions of the shock lying in front of the image plane, whereas the dashed lines indicate the portions located behind the image plane. Right column: projection of the ellipsoid shock front onto the ecliptic plane as seen from the north ecliptic pole. Gray lines depict the 3D structure of the ellipsoid, while the solid and dashed lines indicate whether the corresponding portions of the shock front lie in front of or behind the ecliptic plane, respectively. The red, green, purple, brown, and light-blue lines indicate the magnetic field lines connecting to STA, Earth, PSP, Mars, and SolO, respectively, computed using the Parker+PFSS method described in Section 4.2 (gray is used for the portion of the field line inside the modeled ellipsoid).

For the period under analysis, these maps are provided at daily cadence.[31] The use of far-side magnetograms provided by PHI represents an improvement with respect to the use of synoptic magnetograms built on the assumption that the far-side magnetic field does not evolve, and old Earth-based magnetogram observations can still be used. This ADAPT/WSA method provides 12 estimations for the footpoint location of the field line connecting to each spacecraft, one for each realization.

The top panel of Figure 7 shows the ADAPT/WSA-derived instantaneous magnetic connectivity on 2024 May 19 at 20:00 UT for the five heliospheric locations considered here that observed the M20 SEP event. These are overlaid on the corresponding ADAPT-GONG+PHI map used to derive the coronal field, and the WSA-derived coronal holes (shaded areas in red for positive and blue for negative polarity). Over the 12 realizations, the footpoints of the field lines connecting to PSP (solid purple circle), SolO (solid light-blue circle), L1 (green star), and STA (solid red circle) showed little variation; thus, only one location is indicated in the top panel of Figure 7. In the case of Mars, we indicate with solid brown circles

[31] https://gong.nso.edu/adapt/maps/special/fdt_preliminary_runs/v2/hmi_fdt/

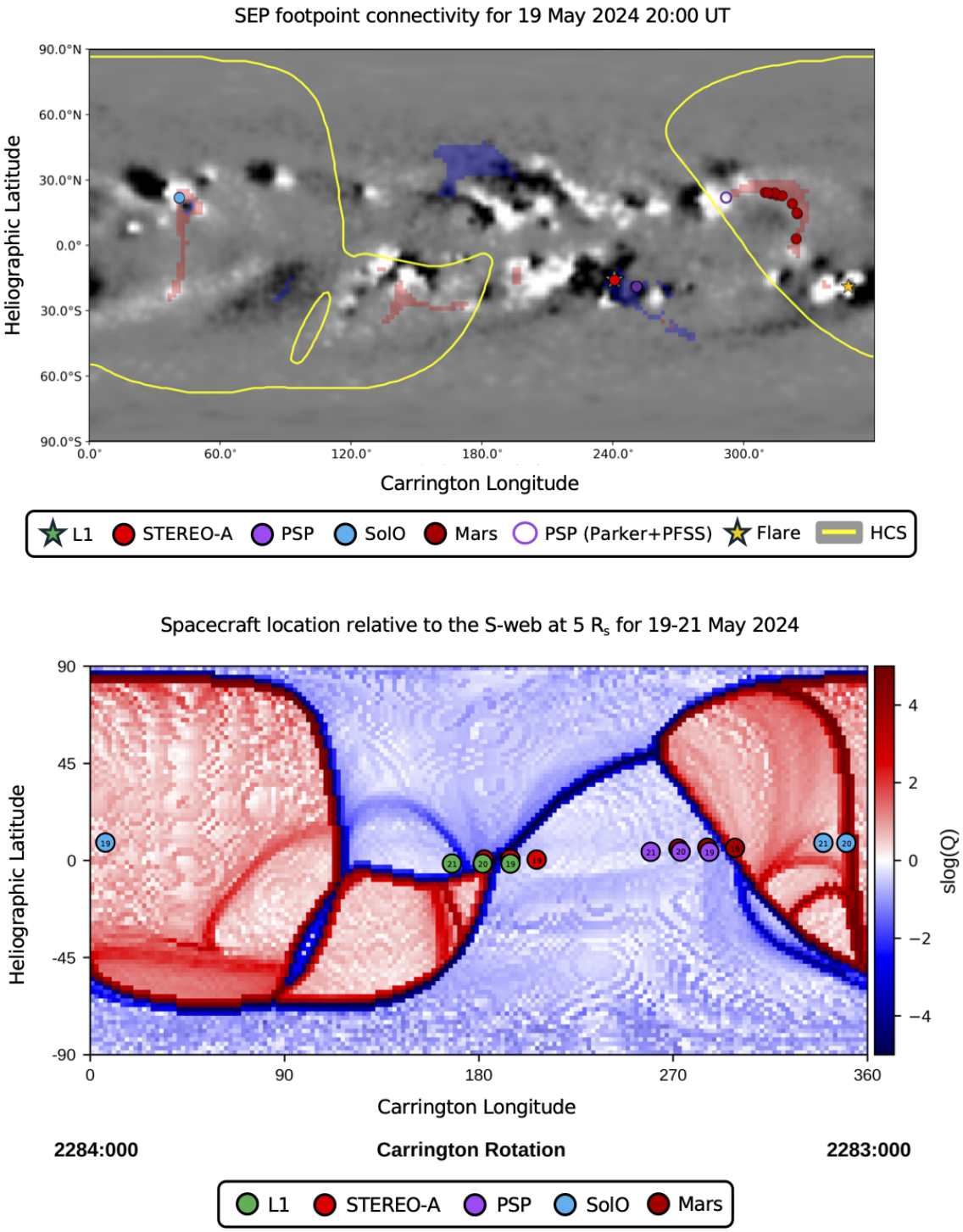

Figure 7. Top panel: ADAPT/WSA-derived instantaneous magnetic connectivity on 2024 May 19 at 20:00 UT for five heliospheric locations observing the M20 SEP event, overlaid on the corresponding ADAPT-GONG+PHI map used to derive the coronal field, and the WSA-derived coronal holes (red is positive; blue is negative). The footpoints of the field lines connecting to PSP, SolO, STA, and L1 are indicated by a solid purple circle, a solid light-blue circle, a solid red circle, and a green star, respectively. The open purple circle indicates the PSP footpoint using the Parker+PFSS method. The solid brown circles indicate the footpoints of the field lines connecting to Mars as obtained by the different ADAPT/WSA realizations. The WSA-derived HCS is overplotted in yellow. Bottom panel: squashing factor at 5 $R_\odot$ for Carrington Rotation 2283 as obtained by the ADAPT/WSA method. The numbered solid circles indicate the location of PSP (purple), SolO (light blue), STA (red), L1 (green), and Mars (brown), for the days May 19, 20, and 21.

several footpoint locations as obtained in the different realizations (all of them lying within a positive-polarity coronal hole at CLs ranging from 310° to 325°).

Table 3 lists the coordinates of the footpoints of the field lines connecting each of the five locations, estimated using the methods discussed above. Column (1) specifies the CL at 05:10 UT on 2024 May 20 of the spacecraft or heliospheric locations where the SEP event was observed, column (2) specifies the solar wind speed used to compute the nominal Parker spiral IMF lines, and columns (3)–(6) specify the

Table 3
Stonyhurst Coordinates and Carrington Longitude of the Magnetic Footpoints

S/C location	V_{sw} (km s^{-1})	Parker	Parker+PFSS	IRAP-ADAPT	ADAPT/WSA
(1)	(2)	(3)	(4)	(5)	(6)
L1 (CL = 178)	408	S02W58 (CL = 236)	S16W62 (CL = 240)	S14W61 (CL = 239)	S16W63 (CL = 241)
STA (CL = 192)	470	S00W60 (CL = 238)	S16W62 (CL = 240)	S14W60 (CL = 238)	S16W63 (CL = 241)
SolO (CL = 348)	509	N07E154 (CL = 024)	N24E139 (CL = 039)	N23E141 (CL = 037)	N22E137 (CL = 041)
PSP (CL = 270)	500	N04W125 (CL = 303)	N22W114 (CL = 292)	N19W111 (CL = 289)	S19W73 (CL = 251)
Mars (CL = 282)	500[a]	N06W167 (CL = 345)	S21W174 (CL = 352)	⋯	N23W136 (CL = 314)[b]

Notes.
[a] Assumed V_{sw} value based on PSP solar wind speed measurements and corotation from PSP to Mars.
[b] Most probable footpoint location based on the 12 ADAPT/WSA realizations.

coordinates of the connectivity footpoints (in Stonyhust coordinates, including the CL) estimated using (3) the Parker method, (4) Parker+PFSS, (5) IRAP-ADAPT, and (6) ADAPT/WSA. The four methods provide consistent results for the L1 and STA footpoints, which were separated by ∼110° in longitude from the site of the X16.5 flare (W171 or CL = 349°; indicated by the orange star in the top panel of Figure 7). When using a coronal magnetic field model (either PFSS or ADAPT), the estimated SolO footpoints using the different methods are also coincident. By contrast, PSP shows the largest discrepancies among the different methods, with the ADAPT/WSA method providing a southern location almost radially aligned with PSP, which questions the validity of this result. The outward magnetic field polarity observed in situ by PSP at the onset of the SEP event (see Section 4.5) suggests that this spacecraft was most likely connected to one of the outward-polarity (red) regions indicated in Figure 7 rather than in an inward polarity (blue) region. For reference, the open purple circle in the top panel of Figure 7 indicates the coordinates of the PSP footpoint using the Parker-PFSS method, which lies in an outward-polarity region. The comparison between the in situ magnetic field polarity measured by each spacecraft and the location of their IMF line footpoints is addressed in Appendix A.

The bottom panel of Figure 7 shows the distribution of the dimensionless quantity slog(Q) as defined in Equation (15) of V. S. Titov et al. (2011), where Q is the "squashing factor." This parameter quantifies the distortion of magnetic field lines, indicating how much magnetic field lines are strengthened and compressed. This slog(Q) distribution (also known as S-web) has been derived from the ADAPT/WSA method at a spherical surface at $R = 5\ R_{\odot}$ and shows regions of opposite polarity, where red (blue) regions correspond to positive (negative) polarities (for the full methodology of deriving the S-web, we refer the reader to S. Wallace et al. 2025). High values of Q identify sharp gradients in the field line mapping formed around separatrix layers and quasi-separatrix layers (QSLs), such as the helmet streamers around the HCS and in pseudostreamers. Low Q values identify regions where the magnetic field is not widely distorted and expands regularly in the solar wind (V. S. Titov et al. 2011). The solid symbols identify the locations of the spacecraft where the M20 SEP event was observed (using the same color code as in the top panel). Numbers inside the symbols indicate the corresponding day in May (19, 20, or 21) for each position. The field polarities in the bottom panel of Figure 7 (at $R = 5\ R_{\odot}$) should be compared with the in situ magnetic field polarities observed a few days later accounting for ballistic solar wind propagation; about ∼2.6 days for PSP and SolO (given the measured solar wind speed at the onset of the event of ∼500 km s^{-1}), and about ∼4 days for STA and L1 (with a solar wind speed of ∼400 km s^{-1}). Notably, all spacecraft were projected to regions close to the S-web, with four of the five spacecraft close to the HCS, and SolO close to an S-web arc that was well separated from the HCS (these separatrices and quasi-separatrices commonly form at pseudostreamers). The flaring region was located at S19 CL = 349°, magnetically connected to a complex S-web topology defined by the vertex of the HCS and several S-web arcs, as seen in the bottom panel of Figure 7, in the southern hemisphere in the CL range ∼320°–360°. The comparison between the in situ magnetic field polarity measured by each spacecraft and the projected polarity in the Q-map is addressed in Appendix A.

4.3. Preevent Interplanetary Context

The methods described in Section 4.2 for estimating the magnetic connectivity of each spacecraft assume a nominal Parker spiral IMF configuration from the spacecraft to a given height above the solar surface. Although commonly used, this approximation may be inadequate during disturbed solar wind conditions, such as those in 2024 May due to the presence of multiple ICMEs.

A large-scale configuration of the IP medium during the M20 SEP event can be obtained from the 3D MHD model of the inner heliosphere developed by D. Odstrčil et al. (1996) known as ENLIL. This code assumes a solar wind background built from WSA simulations driven by a sequence of GONG magnetograms. Transient structures such as CMEs are injected at the inner boundary of ENLIL (at $R = 21.5\ R_{\odot}$) following the "cone model" approach (e.g., D. Odstrcil et al. 2004, 2020; M. L. Mays et al. 2015; and references therein). In this approach, a CME is injected as a spherical expanding plasma cloud introduced as a pressure pulse at 21.5 $R_{\odot}$, characterized by its speed $V_{\rm CME}$, latitude and longitude of the direction followed by the center of the CME, and its angular half-width $\omega_{1/2}$, but without any internal magnetic field structure. We performed an ENLIL simulation using as input CCMC/DONKI CME parameters with speeds >800 km s^{-1} from 2024 May 4 to May 25, derived in near-real time by M2M/SWAO analysts, as listed in Table 2. This simulation was executed using CCMC Runs-On-Request. Details including movies are available online.[32]

[32] https://ccmc.gsfc.nasa.gov/ror/results/viewrun.php?runnumber=David_Lario_051925_SH_2

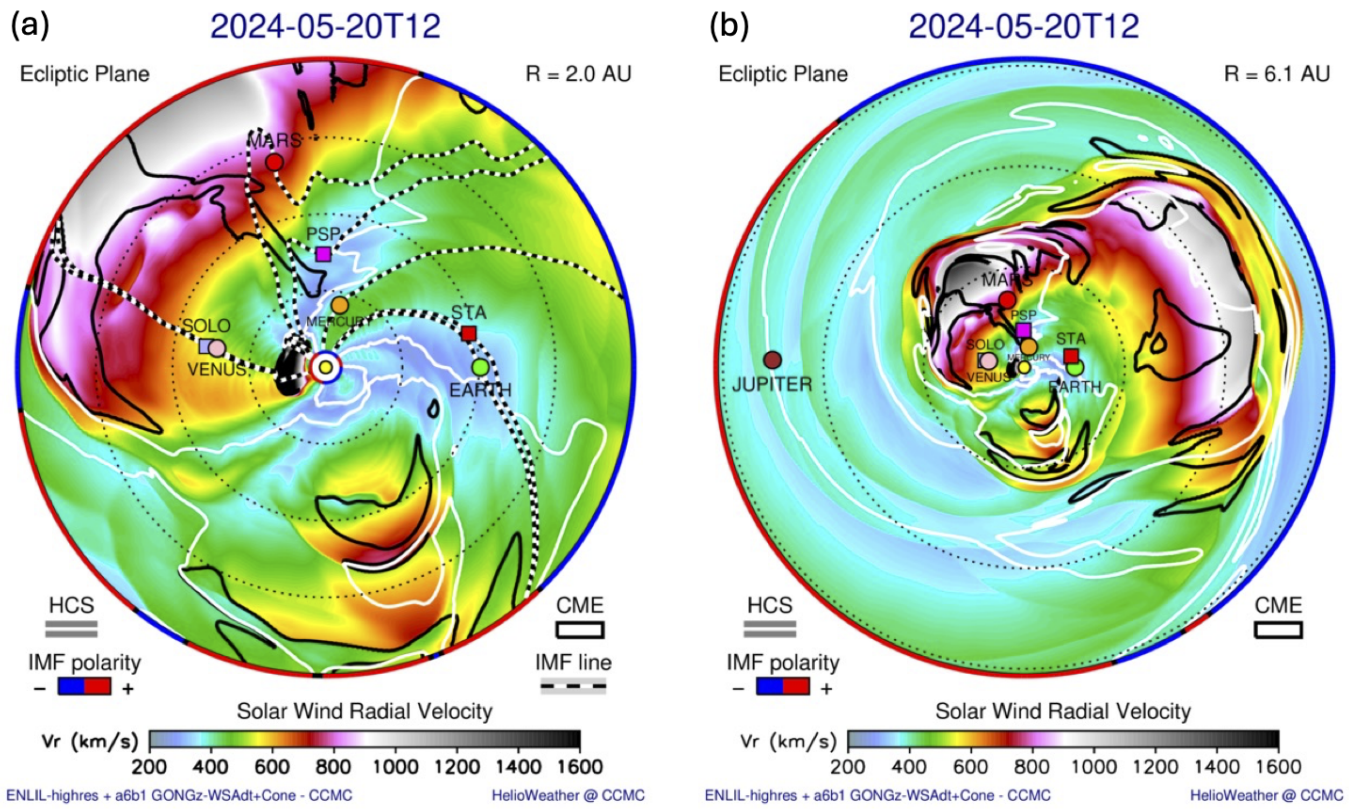

Figure 8. Solar wind speed contours at the ecliptic plane on 2024 May 20 at 12:00 UT as obtained from the ENLIL simulation up to a distance (a) $R = 2.0$ au and (b) $R = 6.1$ au. The simulation includes all DONKI CMEs listed in Table 2 up to May 25. The black contours track the density of the injected pulses as they deform and merge when propagating in IP space. In the left panel, the white–black-dashed lines indicate the field lines connecting to the different spacecraft and planets (including Mercury, Mars, and Venus). Field lines are removed from panel (b) to better visualize the location of the CMEs.

Figure 8 shows two snapshots of the simulated solar wind velocity in the ecliptic plane up to a distance (a) $R = 2.0$ au and (b) $R = 6.1$ au on 2024 May 20 at 12:00 UT. The black contours trace the CME density after injection at the simulation in the inner boundary. At the time of the snapshots, the CME origin of the M20 SEP event was already in the ENLIL domain, visible as the black contour at ∼0.25 au propagating toward SolO, whereas all the prior CMEs propagated to larger heliocentric distances. Figure 8(b) shows that the Earth-directed CMEs responsible for the intense geomagnetic storms at Earth on May 10–11 were already at distances $\gtrsim$5 au by the time of the M20 SEP event. The continuous CME activity from AR 13664, as it rotated over the west limb of the Sun (as seen from Earth), resulted in a merged wrapping structure spanning nearly ∼180° in longitude. Additional CMEs originated from other ARs (see Table 2) propagated toward the east limb of the Sun (as seen from Earth) at distances $R \lesssim 2$ au. It should be emphasized that, in this simulation, CMEs were injected using the cone approximation without any internal magnetic field structure. As a result, the configuration of the IMF lines within these structures (displayed by black- and white-dashed lines in Figure 8(a)) most likely differs from the actual IMF topology existing at the time of the M20 SEP event.

4.4. Radio Observations

Figure 9(a) displays the dynamic spectra of the radio observations as measured by (from top to bottom) PSP/FIELDS, SolO/RPW, STA/SWAVES, and Wind/WAVES. An intense multicomponent type III radio burst with onset at 05:14 UT was first detected at the highest frequencies (∼16 MHz) of the PSP and SolO radio instruments. By contrast, the multicomponent type III radio burst at STA and Wind was much weaker, with prominent emission starting at lower frequencies ($\lesssim$5 MHz) at about 05:16 UT. This weaker and delayed radio emission at Wind and STA suggests that its solar origin was located on the far side of the Sun from STA and Wind points of view and resulted from occultation of the high frequencies by the solar limb. At PSP, clear signatures of local Langmuir waves were observed between ∼05:50 UT and 06:00 UT, indicating that the electron beams causing the type III radio emissions were able to reach PSP. Intermittent signatures of type II radio bursts were also detected by all four spacecraft, being most intense at PSP. At SolO, spacecraft-related electromagnetic interference (M. Maksimovic et al. 2021) made the type II burst more difficult to observe. At PSP, the type II emission started at the highest frequencies of the FIELDS instrument at about ∼05:25 UT and can be tracked up to ∼06:15 UT at ∼1.8 MHz. At Wind, the signatures of the type II burst did not start until ∼05:38 UT probably due to solar occultation.

By fitting the radio peak fluxes observed by the four spacecraft at different frequencies with a circular Gaussian distribution, it is possible to estimate where the emission of the type III radio burst originated (see details in V. Krupar et al. 2024). We use the radio peak fluxes at the frequencies 875, 775, and 675 kHz. The selection of these frequencies is based on (i) the quality of data at the different spacecraft, (ii) the fact

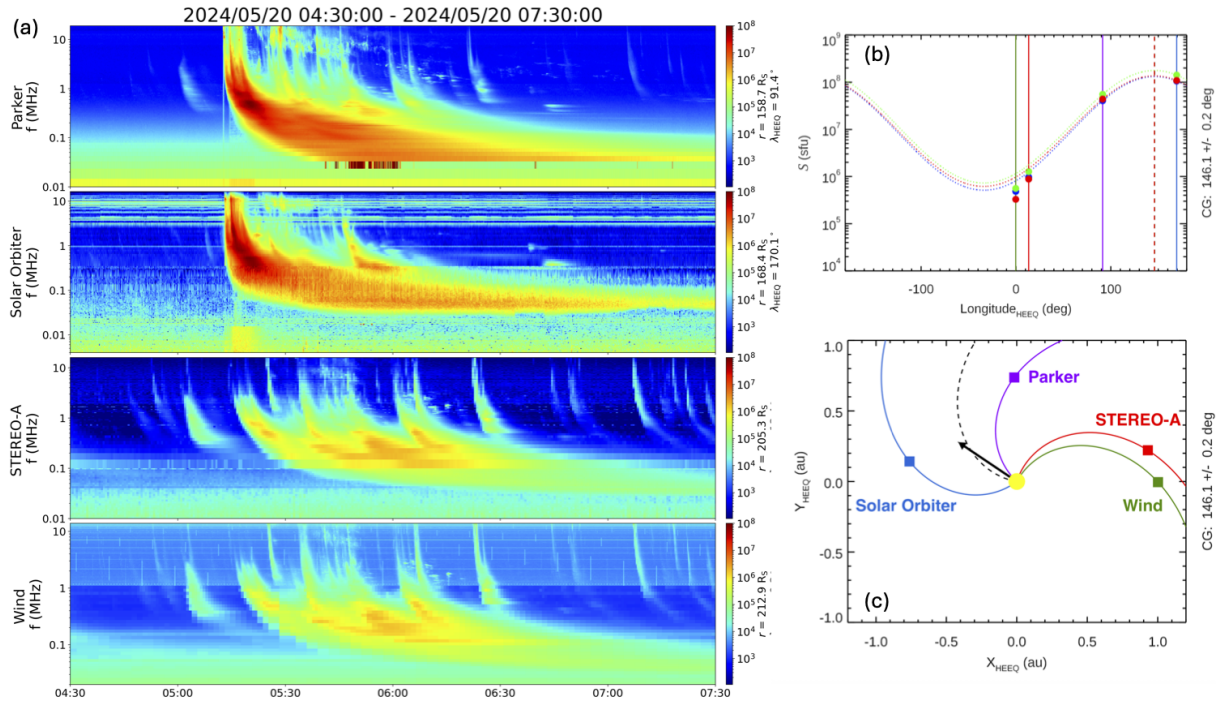

Figure 9. (a) Radio emission detected by (from top to bottom) PSP, SolO, STA, and Wind. (b) Radio intensity distribution across spacecraft locations (indicated by the vertical solid lines, green for Wind, red for STA, purple for PSP, and light blue for SolO) for the first and most intense type III radio bursts (with 875 kHz onset at 05:15 UT at SolO and PSP, but 05:17 UT at STA and Wind). The intensity of the radio emission for five distinct frequency channels is represented by colored circles (red 875 kHz, green 775 kHz, blue 675 kHz). The dotted curves illustrate the fitting results derived using the method described in V. Krupar et al. (2024). The dashed vertical lines indicate the determined direction for each frequency (in this specific case, all analyzed frequencies yield the same direction). (c) Spatial distribution of spacecraft (colored squares) and radio source of the type III radio burst in the HEEQ coordinate system (the $X_{\rm HEEQ}$–$Y_{\rm HEEQ}$ plane). Parker spiral IMF field lines connecting each spacecraft with the Sun are plotted assuming a solar wind speed of 470 km s^{-1}. A particular Parker spiral, originating from the solar flare site at W171, is emphasized using a black-dashed curve. The black arrow indicates the determined direction at W146.

that Wind/WAVES offers calibrated radio flux measurements only up to 1040 kHz, and (iii) STA and Wind detected the type III radio burst only at low frequencies. Applying the method developed by V. Krupar et al. (2024) to the first and most intense component of the type III radio burst, Figure 9(b) shows the longitudinal fit of the radio peak fluxes at the three selected frequencies, with the maximum at the longitude indicated by the vertical dashed lines. Averaging over the three selected frequencies, we estimate an average direction associated with the maximum radio flux at 146.1°±0.2°. We note that, whereas the parent AR was located at W171 (Table 1), the apex of the ellipsoid fitted to the CME coronagraph images propagated along the W164 direction (Section 4.1), and the beam of electrons producing the type III radio burst was most likely centered around W146.

4.5. Details of the M20 SEP Intensity Profiles at SolO, PSP, STA, and L1

The two top panels of Figure 10 show the ion intensity-time profiles as measured by (left) SolO and (right) PSP from 2024 May 19 to May 30. These two spacecraft were on the far side of the Sun and better connected to the solar event than L1 and STA (e.g., Figures 5, 7, and 9). In particular, the top left panel shows ion intensities measured by the Sun aperture of SolO/EPT (energies below 5.31 MeV), and proton intensities measured by the Sun aperture of SolO/HET (energies above 7.62 MeV). Note that, during this period, the onboard SolO/EPD software used an outdated temperature configuration that affected the onboard EPT and HET calibration tables (A. L. Kollhoff 2025). Because data recalibration into physical units was not possible for all energies, the energy coverage of the particle intensities in the top left panel of Figure 10 was not continuous. The top right panel of Figure 10 displays proton intensities measured by PSP/EPI-Lo obtained from the ChanP product averaged over all EPI-Lo apertures excluding those affected by dust impacts or field-of-view obstructions[33] (energies below 607 keV), and the A apertures of PSP/EPI-Hi/LET (energies between 1.30 and 8.72 MeV) and of PSP/EPI-Hi/HET (energies above 10.37 MeV). Because of its low geometric factor, EPI-Lo/ChanP requires high particle intensities to trigger its count rates, resulting in a gap in the almost continuous energy coverage between EPI-Lo/ChanP and EPI-Hi/LET-A intensities on May 26 and 27 when the particle intensities of the M20 SEP event decayed below the EPI-Lo/ChanP sensitivity threshold.

The three bottom left and bottom right panels of Figure 10 show the magnetic field magnitude and RTN angular directions as measured by SolO/MAG and PSP/FIELDS/MAG, respectively. The horizontal red lines indicate the angular directions for a nominal IMF Parker spiral configuration at $R = 0.78$ au (left) and $R = 0.74$ au (right) assuming the solar wind speed ∼500 km s^{-1} measured at the onset of the SEP event with the two different polarities labeled *OUT* and *IN* in the bottom panels. The solid vertical lines indicate the passage of IP shocks. The gray-shaded bar in the left panels indicates the passage of the ICME counterpart of the CME on 2024 May 20 (Figure 6). This ICME was observed in situ only by SolO. The shock associated with this ICME was observed

[33] See https://spp-isois.sr.unh.edu/Release-Notes.html.

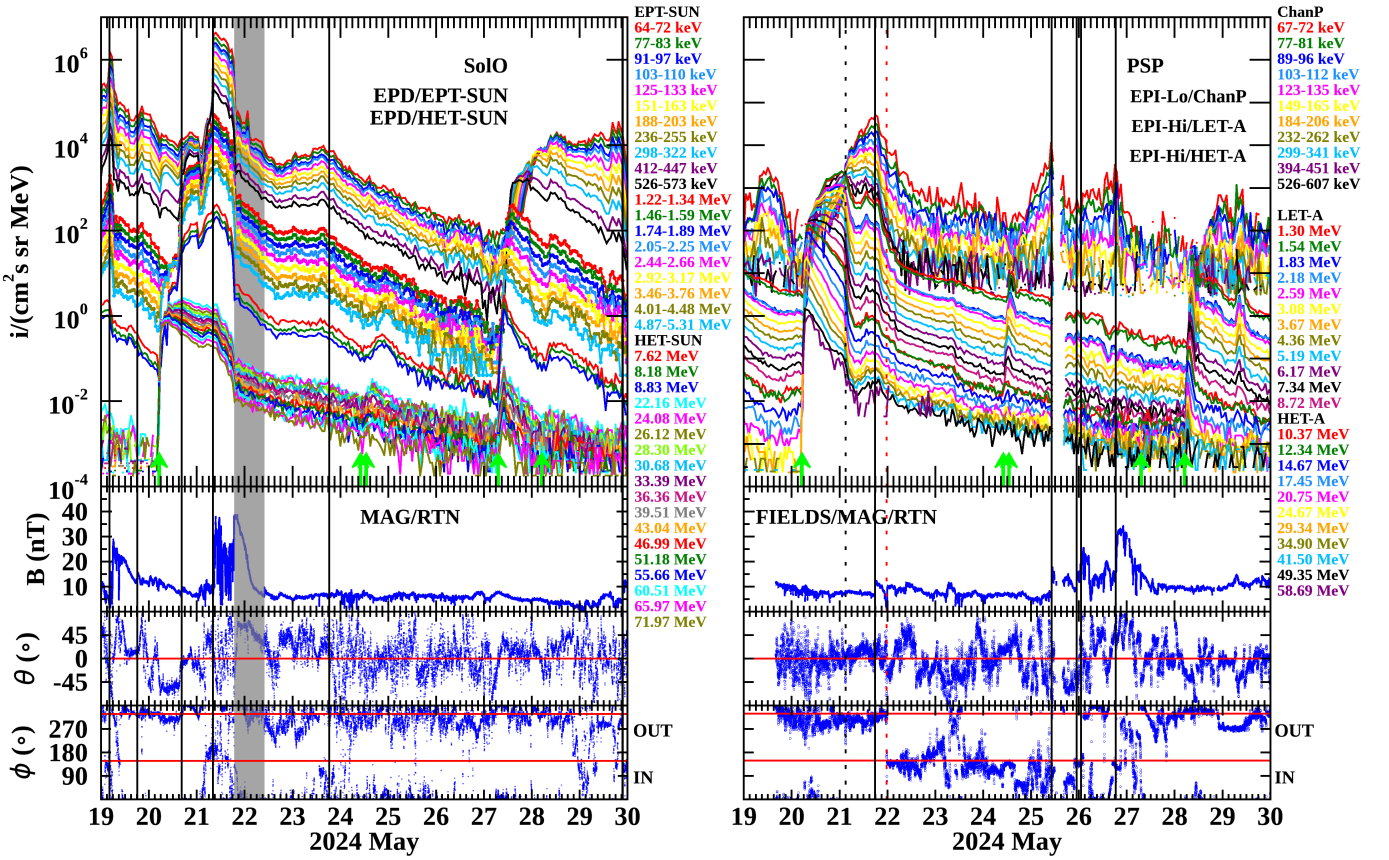

Figure 10. Energetic ion intensity-time profiles during the 2024 May 20 SEP event, together with the magnitude and angular directions (in RTN spacecraft-centered coordinates) of the magnetic field as observed by (left) SolO and (right) PSP. The solid vertical lines indicate the passage of IP shocks, and the shaded gray bar the passage of an ICME detected by SolO. The black- (red-) dotted line in the PSP panel indicates a discontinuity in the particle intensities at 03:00 UT (the crossing of a magnetic field sector boundary at 23:35 UT) on 2024 May 21. The green arrows in the top left and top right panels indicate the occurrence of the most intense type III radio bursts observed throughout the plotted period by both SolO and PSP.

by SolO at 08:09 UT on May 21, and presumably by PSP at 17:45 UT on May 21. The longitudinal separations of PSP ($\Delta\Phi \sim 80°$) and SolO ($\Delta\Phi = 1°$) with respect to the site of the parent solar eruption are consistent with the propagation direction inferred from the modeling of the CME-driven shock in the right column of Figure 6 suggesting that the CME-driven shock impacted SolO near its apex, whereas only a flank was observed by PSP (see Section 5.3).

This potential head-on ICME impact at SolO raises questions about possible (geo)magnetic effects had this ICME encountered Earth. Despite its speed and favorable trajectory, estimates of the Dst index using the R. K. Burton et al. (1975) and the T. P. O'Brien & R. L. McPherron (2000) models (see applications of these models to other events in E. Paouris et al. 2023, 2025) provide minimum Dst values around ~ -100 nT during the passage of the ICME sheath and later during the passage of the wake of the ICME, while during passage of the main body of the ICME, where the magnetic field was mostly northward, minimum values of Dst would have been above -50 nT (not shown here). Interestingly, this ICME also originated in AR 13664, which gave rise to the interacting ICMEs that caused the geomagnetic storms on 2024 May 10–11 with minimum Dst ~ -406 nT (S. Khuntia et al. 2025), yet despite being less geoeffective, it was associated with a more intense X-ray flare and a faster CME. Possible reasons include that this CME was isolated and that its embedded magnetic field was predominantly northward.

The green arrows in the top left and top right panels of Figure 10 indicate the occurrence of major type III radio bursts detected by both SolO and PSP during the period May 19–30. The most intense type III bursts were associated with the large flares and CMEs on 2024 May 20 (Section 4.4) and 2024 May 27 (Tables 1 and 2). The type III radio burst at ~05:05 UT on 2024 May 28 was associated with an M2.2 flare located at S22W156 peaking at 05:10 UT as observed by STIX and a halo CME at 05:24 UT but with only a $V_{POS} \sim 675$ km s^{-1} (because of the flare intensity and CME speed, this event was not listed in Tables 1 and 2). The type III radio burst at ~10:02 UT on 2024 May 24 was most likely associated with an EUV brightening located at N19W167 observed by SolO/EUI/FSI between the images collected at 10:00 UT and 10:15 UT. The type III radio burst at ~12:56 UT on 2024 May 24 was most likely associated with an M9.8 flare at S19E130 peaking at 12:57 UT as observed by STIX and a partial-halo CME at 13:25 UT with PA $= 95°$, $\omega_{POS} = 207°$, but only $V_{POS} \sim 550$ km s^{-1} (because of its low speed, this event was not listed in Table 2). Except for the type III burst on May 27, which did not translate to any additional proton intensity enhancement at PSP (probably poorly connected because of its origin at S10E109), all type III radio bursts coincided with relatively small enhancements in $\lesssim$60 MeV proton intensity observed by both SolO and PSP during the decay of the M20 SEP event.

The ion intensity-time profiles of the M20 SEP event at SolO are typical of an SEP event associated with an eruption

near the central meridian relative to the observing spacecraft (e.g., H. V. Cane et al. 1988). The peculiarities of the event at SolO include (i) the changing and out-of-the-ecliptic field orientations observed during the rising phase of the SEP event; (ii) the crossing of an IP shock at 16:22 UT on May 20 that affected the rising phase of the SEP event at energies $\lesssim$8 MeV; (iii) the intensity increase associated with the IP shock driven by the M20 CME that was observed even at energies $\gtrsim$70 MeV; (iv) the intensity depression at the entry of SolO into the ICME ejecta observed at all plotted energies; (v) the unrelated shock at 18:27 UT on May 23 that was accompanied by an increase in the $\lesssim$8 MeV proton intensities during the decay phase of the M20 SEP event; and (vi) a small intensity increase, even at energies ~60 MeV, associated with the aforementioned solar eruptions on May 24 superimposed on the decay of the M20 event. The new SEP injection related to the flare and CME on 2024 May 27 produced a prompt intensity increase that, at proton energies $\gtrsim$20 MeV, reached a rapid peak followed by a fast decay. After this decay, $\gtrsim$20 MeV proton intensities continued decreasing with the same rate as during the M20 SEP event, contributing to extend the energetic particle reservoir observed in Figure 4.

The ion intensity-time profiles of the M20 SEP event at PSP (top right panel of Figure 10) are typical of SEP events associated with solar eruptions on the western hemisphere of the Sun relative to the observer, i.e., from well-connected longitudes with a prompt rapid onset leading to a peak followed by a slow gradual decay (e.g., H. V. Cane et al. 1988). The peculiarities of the M20 SEP event at PSP include (i) the simultaneous proton intensity drop at energies $\gtrsim$1.3 MeV but increase at lower energies (indicated by the black, vertical dotted line in the right panels of Figure 10) at 03:00 UT on May 21. This ion intensity discontinuity did not coincide with any clear local magnetic field discontinuity, suggesting that probably PSP just entered a flux tube with a completely different energy spectrum than those observed during the rising phase of the SEP event. A possible interpretation is that the particle source was discontinuous along the CME-driven shock front. Additional peculiarities of the M20 SEP event at PSP are (ii) the passage of the shock at 17:45 UT on May 21, which despite its small magnetic field increase was accompanied by proton intensity increases even at ~50 MeV, (iii) the magnetic sector boundary crossing at 23:35 UT on May 21 with IMF polarity changing from outward to inward (indicated by the vertical red-dotted line), which coincided with a drop in the $\lesssim$300 keV proton intensities but practically no change at higher energies, (iv) the small proton intensity increase at energies $\lesssim$15 MeV associated with the aforementioned solar eruptions on May 24, which interrupted the decay of the M20 SEP event at these energies, and (v) the arrival of an enhanced magnetic field structure on May 26, probably related to the passage of a solar wind stream interaction region formed ahead of a high-speed ($\gtrsim$500 km s^{-1}) solar wind stream observed on May 27–28 (not shown here), which modified the $\lesssim$1 MeV proton intensity profiles. The intensity increase on May 28 associated with the M2.3 flare from S22W156 was very brief at energies $\gtrsim$15 MeV. Shortly after this increase, the proton intensities at these energies decayed at the same rate as during the M20 SEP event, extending the energetic particle reservoir (Figure 4).

The two top panels of Figure 11 show the ion intensity-time profiles from 2024 May 19 to May 30 as measured by (left) near-Earth spacecraft (i.e., ACE and SOHO) and (right) STA. In the top left panel, we plot ion intensities from selected energy channels of ACE/EPAM/LEMS120 (energies below 1.91 MeV), SOHO/EPHIN (the 4.3–7.8 MeV proton energy channel, orange trace), and SOHO/ERNE (energies above 13.8 MeV). In the top right panel, we combine data from the Sun aperture of STA/SEPT (energies below 1.265 MeV), STA/LET (energies between 1.8 and 10 MeV), and STA/HET (energies above 13 MeV). During the plotted period, the ion intensity-time profiles at energies $\lesssim$15 MeV were dominated by the decaying intensities from prior SEP events (see Figure 2). The particle intensity increase on 2024 May 20, presumably associated with the far-side solar eruption analyzed in Section 4.1, was clearly observed at energies $\gtrsim$20 MeV. This increase showed a gradual rising phase, reaching a maximum late on May 20 or early on May 21 (depending on the energy), followed by a slow decay extending beyond May 30 (see Figures 2 and 4). The gradual increase occurred about ~3–4 hr after the onset of the X16.5 flare and was characterized by very low anisotropies (see Appendix B). One peculiarity of this SEP event at both L1 and STA was that proton intensities at energies between ~30 and ~80 MeV were very close in value and evolving similarly in time throughout the decay phase of the SEP event, at least until May 28 (Appendix C describes the evolution of the ion energy spectra at both L1 and STA).

Throughout the development of this SEP event at both L1 and STA, the solar wind and IMF remained relatively quiet, without significant transients, shocks, or solar wind speed excursions (Figure 2). The only exception was the passage of ICMEs at STA indicated by the gray-shaded bars in the right-hand panels in Figure 11, as reported by the Helio4cast catalog (C. Möstl et al. 2017, 2020).[34] These ICMEs probably originated in association with $\leqslant$ M5 flares on May 23 or May 24 from AR 13679 at western longitudes as seen from Earth. A possible candidate is the LASCO CME at 13:25 UT with V_{POS} = 527 km s^{-1} at PA = 242° and ω_{POS} = 116° temporally associated with an M2.5 flare from S09W65 peaking at 13:20 UT on May 23. Notably, no ICMEs at L1 were reported in either the Helio4cast or the NEICMEs catalogs.

5. Discussion: Energetic Particle Access to L1 and STA

The long-lasting elevated $\gtrsim$100 MeV proton intensities observed near Earth, together with the observation of the widespread particle reservoir, and the flattening of the energy spectrum at energies ~30–80 MeV, make this event an excellent case to investigate the key mechanisms behind the spread of SEPs in the inner heliosphere. Among the different mechanisms invoked to explain the spread of SEPs in the heliosphere (see Section 1), in this section, we consider those that may have contributed to the near-Earth observation of the M20 SEP event. In particular, we consider whether the possible particle sources were directly connected with the observing spacecraft, whether efficient cross-field transport processes or other SEP transport effects were necessary to explain the particle enhancements at L1 and STA, and/or whether particle reflection and redistribution by the merging of

[34] https://helioforecast.space/icmecat; doi: 10.6084/m9.figshare.6356420.

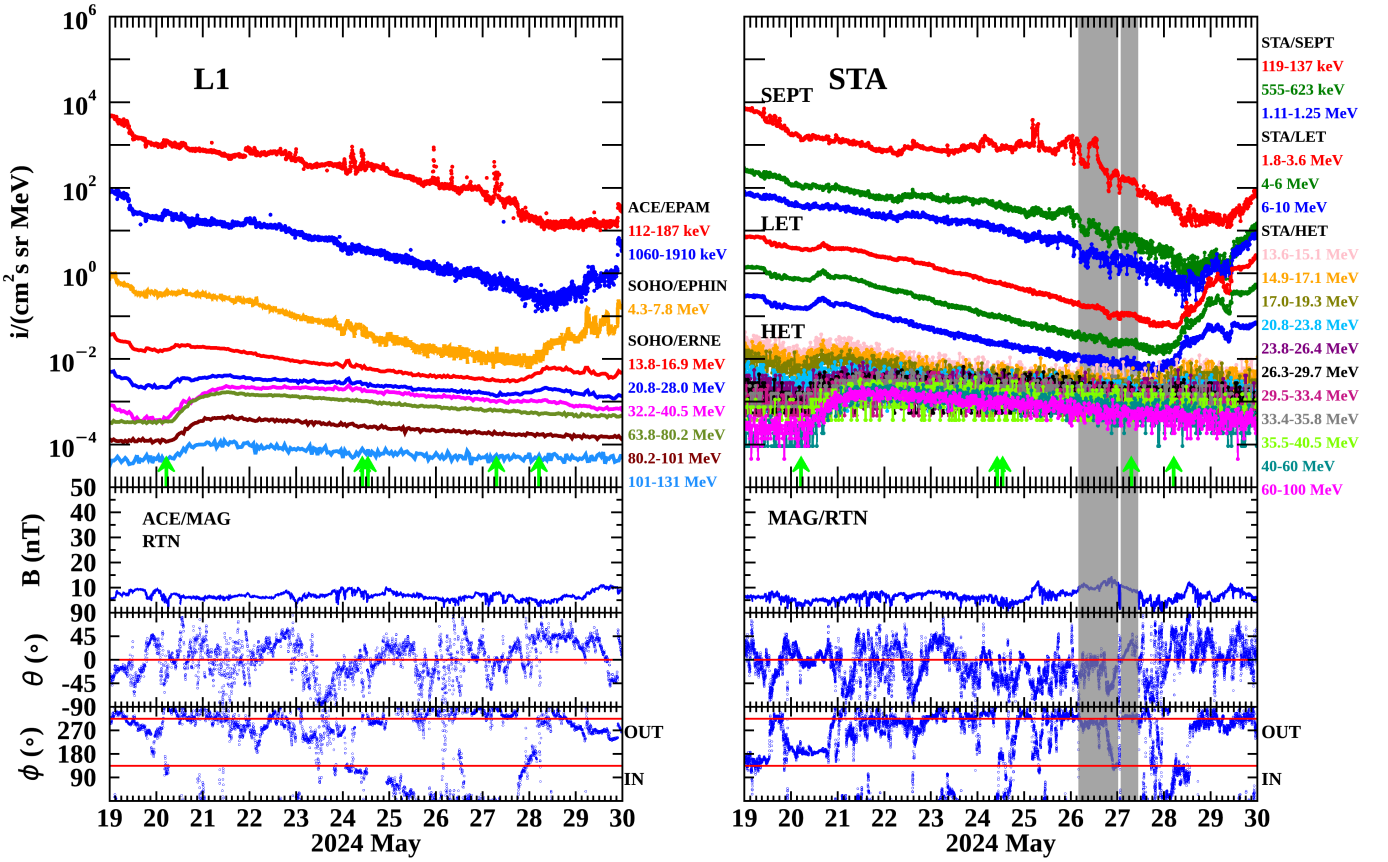

Figure 11. Energetic ion intensity-time profiles during the 2024 May 20 SEP event, together with the magnitude and angular directions (in RTN spacecraft-centered coordinates) of the magnetic field as observed by (left) spacecraft at L1 (i.e., ACE and SOHO) and (right) STA. The shaded gray bars indicate the passage of ICMEs as reported in the Helio4cast catalog. The green arrows in the top left and top right panels indicate the occurrence of type III radio bursts as in Figure 10.

prior CMEs located beyond 1 au played a role (see references in Section 1 for details on these mechanisms).

5.1. Particle Sources Magnetically Well Connected to L1 and STA

One of the factors to consider in the observation of SEPs by a spacecraft is whether magnetic connection between the particle sources and the spacecraft is established (e.g., D. Lario et al. 2017a; and references therein). For a near-Earth spacecraft, the nominal magnetic connection is usually established to the western hemisphere of the Sun. The methods used in Section 4.2 determined that both L1 and STA were magnetically connected around W60 relative to Earth (Table 3). Therefore, we first examine the solar activity phenomena occurring on the Earth-facing side of the Sun, and in particular whether there is any evidence for an additional particle source that might have contributed to the M20 SEP event as observed at L1 and STA.

As described in Section 4.1, the only solar eruption occurring near that region that could be the origin of the energetic particle intensity increase observed at L1 and STA was the EUV brightening extending in a narrow range of longitudes southward of S20 associated with a short-duration C6.7 flare from AR 13683 at ∼S20W66, with onset at 05:42 UT, peaking at 05:54 UT, and ending at 06:16 UT on May 20. The association of this EUV brightening with a WL CME was difficult to establish, since no clear EUV signatures of an eruption extending above the solar limb were observed by SDO/AIA, STA/EUVI, or SolO/EUI/FSI. Nevertheless, in the LASCO/C2 direct images, a narrow ($\omega_{POS} \sim 30°$), slow ($V_{POS} \sim 678$ km s^{-1}) WL structure was visible, first appearing at 05:48 UT propagating southwestward (PA∼210°), superposed on the main backside halo CME associated with the X16.5 flare seen in LASCO/C2 images, although it was not identified as a separate CME in any catalog. The detection of a type III radio burst in association with this EUV brightening and C6.7 flare is also uncertain because of the ongoing type III storm at that moment (Figure 9). The arrival of high-energy protons at L1, which observations suggest had an isotropic distribution (see Appendix B), occurred after ∼08:00 UT on May 20. This timing suggests that, if they originated with the C6.7 flare or the narrow CME structure, they would have had to have been injected much later than the onset of the EUV brightening. Alternatively, (i) L1 and STA may have been magnetically connected to a region distant from the site of the C6.7 flare, producing a delay before the mobile source established magnetic connection with L1 and STA, and/or (ii) SEP transport to L1 and STA took longer than expected for a direct Parker spiral IMF connection to the source. Overall, the modest intensity of the C6.7 flare, the facts that no EUV signature was seen above the solar limb, and that the only possible WL signature was a narrow, slow CME propagating mostly southward make it difficult to attribute the $\gtrsim$100 MeV protons observed near Earth for over 2 weeks to this EUV brightening, although a minor contribution to the SEP population cannot be excluded.

Statistical studies indicate that the probability of observing SEP events over a wide range of heliolongitudes is larger for solar eruptions associated with X-class solar flares (I. G. Richardson et al. 2026), and with fast (V_{POS} > 1000 km s^{-1}) and wide (ω_{POS} > 120°) CMEs (e.g., D. Lario et al. 2020; I. G. Richardson et al. 2026 and references therein). These criteria were not met by the eruption associated with the C6.7 flare. Therefore, the most likely candidate for the origin of the high-energy particle enhancement observed near Earth is the shock driven by the backside halo CME on 2024 May 20 (V_{POS} ~ 1459 km s^{-1} according to the CDAW LASCO catalog, although CCMC/DONKI reported V_{POS} ~ 2678 km s^{-1} when using the SWPC/CAT method applied to the CME shock identification; see Table 2). However, the challenge is then to understand the processes that transport high-energy SEPs from this far-side event to L1 and STA.

Magnetic connection between the CME-driven shock and the spacecraft would facilitate the observation of the SEPs. However, the reconstruction of the shock driven by the CME (right column of Figure 6) suggests that STA and L1 barely established direct magnetic connection with the geometrical shape assumed in the shock reconstruction. The fact that only L1 and STA coronagraph images (separated by ~13° in longitude) were used in the CME-shock reconstruction, as well as the assumption of an hypothetical geometrical shape to represent the large-scale structure of the shock, makes this shock reconstruction an approximation to the actual shock structure. It is possible that the shock extended farther than is shown in Figure 6, allowing STA and L1 to connect with the shock. The hypothetical connection of STA and L1 with the shock would have to be established with the west flank of the shock and occur in such a way that (i) the shock did not leave any clear EUV signature over the Earth-facing side of the solar disk as no propagating EUV perturbation was seen on the disk by SDO/AIA, (ii) protons arrived at L1 and STA with a delay of ~3–4 hr with respect to the onset of the X16.5 flare, and (iii) proton fluxes at L1 were apparently isotropic (see Appendix B). Additionally, sustaining the elevated ≳100 MeV proton intensities at L1 for an extended period of time would require that the flank of the shock connected to L1 continuously accelerated ≳100 MeV protons as it propagated into IP space. The fact that no IP shock was observed in situ by either STA or L1 spacecraft suggests that, if such magnetic connection existed, at some point the shock flank connected to L1 and STA either weakened, dissipated, or became disconnected from these spacecraft. Even if the flank of the CME-driven shock established magnetic connection with both STA and L1 and the conditions were appropriate to accelerate high-energy protons and thus produce the onset of the SEP event at both STA and L1, transport processes rather than direct magnetic connection with the shock were most likely responsible for both the delayed isotropic arrival of particles and the long decay of high-energy SEP intensities at both STA and L1.

5.2. Effects of the S-web

The squashing factor Q shown in the bottom panel of Figure 7 quantifies how strongly neighboring magnetic field lines diverge. High-Q regions mark QSLs where the magnetic field shows large variations with a small change in location, implying strongly varying field connectivity, but also regions of possible magnetic reconnection. N. A. Schwadron et al. (2026) showed that localized magnetic reconnection along high-Q regions may effectively accelerate particles. Such acceleration processes may occur in regions of strong magnetic field gradients such as in QSLs even in the absence of strong expansions or compressions in density (N. A. Schwadron et al. 2026). The result is the formation of accelerated particle populations aligned with the high-Q regions. Interaction of a CME-driven shock with QSLs may facilitate the escape of particles from the high-Q regions into IP space, whereas those in regions unaffected by the CME-driven shock need additional magnetic reconnection, or alternatively cross-field diffusion or gradient and curvature drifts to escape into IP space (N. A. Schwadron et al. 2026).

The bottom panel of Figure 7 shows that both L1 and STA were located in the direction of high-Q regions created along the HCS in a zone parallel to the ecliptic plane. The question is whether the CME-driven shock (originated at S19 CL = 349°) extended sufficiently to reach these regions, use the particles in QSLs as seed population, and thus facilitate the escape of the particles. However, both solar observations and CME-shock reconstruction provide no evidence (Section 4.1) that the CME-driven shock reached CL ~ 240°, where the different connectivity methods estimate that L1 and STA footpoints were located (Table 3), nor that it intercepted the IMF lines connected to L1 and STA at higher altitudes.

On the other hand, SEP transport models (e.g., C. O. G. Waterfall et al. 2022, 2025; A. Moradi & J. Giacalone 2022, 2025) suggest that, when the solar source is close to the HCS, particle drifts can lead to large longitudinal displacements of particles along the HCS. Indeed, even when spacecraft are poorly connected to the parent AR, the proximity of the AR to the HCS has been suggested as a mechanism for the particles to spread at different longitudes, and thus be observed by spacecraft at poorly connected locations when they come closer to the HCS (see C. R. A. Augusto et al. 2019; and C. O. G. Waterfall et al. 2022 for the case of GLEs). The bottom panel of Figure 7 shows that both STA and L1 were positioned to intercept the HCS as it propagated from 5 $R_\odot$ to the spacecraft location (see discussion in Section 4.2 and Appendix A). The extent of the CME-driven shock (starting at S19 CL = 349°) could have injected particles onto the HCS, which then acted as a conduit for the particles to reach STA and L1 and thus be observed when the HCS intercepted these locations a few days later. In principle, the pseudostreamers would be less efficient in spreading particles via drifts, because strong magnetic field gradients are more easily maintained if there are large field misalignments such as in regions of opposite polarity like in the HCS. Whereas the web of magnetic field polarity separators helps to broaden the longitudinal spread of particles, the close proximity of L1 and STA to the HCS may facilitate the arrival of SEPs at these locations, although signatures of HCS interception were only seen ~4 days after the X16.5 flare (see Figure 11 and Appendix A). Therefore, the effect of the S-web may explain the spread of particles over large angular separations, but the arrival of the first particles at L1 and STA a few hours after the occurrence of the X16.5 flare when neither STA or L1 were in the drift direction is difficult to achieve via this mechanism. Nevertheless, particle drifts along the HCS may explain the later arrival of high-energy particles when L1 and STA became closer to the HCS and thus prolong the decay of the M20 SEP event.

5.3. CME-driven Shock Acceleration and Cross-field SEP Transport

In this section, we use an SEP model that includes (i) MHD simulations of both the background solar wind medium where SEP events develop, and the propagation of CME-driven shocks in IP space, (ii) diffusive shock acceleration of particles at the CME-driven shocks, and (iii) transport of the shock-accelerated particles in the inner heliosphere. Specifically, we use the 2D improved Particle Acceleration and Transport in the Heliosphere (iPATH; J. Hu et al. 2017, 2018; Z.-Y. Ding et al. 2020; Z. Ding et al. 2022) as implemented to run in real time at the Integrated Space Weather Analysis (ISWA) application[35] of NASA/CCMC. All model inputs, including solar wind and CME parameters, field turbulence, and suprathermal seed particle parameters, are automatically retrieved from CCMC online databases, without human intervention.[36]

In particular, iPATH models the background solar wind and CME-driven shocks at the ecliptic plane, starting at $R = 0.05$ au, using the 2D MHD ZEUS code.[37] The real-time iPATH uses 8 hr averaged solar wind data to generate a simplified uniform ambient solar wind (for example, the magnetic field turbulence characterized by $\delta B^2/B^2$ and used in the SEP transport model is obtained from measurements at L1 prior to the event and scaled with heliocentric distance as $\delta B^2 \propto r^{-3.5}$). Shocks are automatically ingested into the ZEUS model as pulse perturbations using CME parameters from the CCMC/DONKI database posted shortly after the occurrence of the solar eruption. The simulation presented here was triggered by the CME with the ID "2024-05-20T05:36:00-CME-001" in the DONKI database.[38] The CME speed was estimated to be 1927 km s^{-1}, with a 43° half-width centered at a longitude $\Phi = 176°$. These CME parameters were based on the application of SWPC/CAT to the CME leading edge (iPATH simulation results using CCMC/DONKI CME parameters based on the shock identification do not differ significantly from those shown here).[39] The colored contour in Figure 12(a) shows a snapshot of the 2D MHD ZEUS simulation of the solar wind density in the ecliptic plane (scaled as R^2) taken 33.4 hr after the initiation of the simulation (i.e., $dt = 33.4$ hr). The black- and white-dashed lines indicate IMF lines connecting Earth (yellow circle), STA (red square), Mars (red circle), PSP (green square), and Venus (green circle) with the Sun (white circle at the center) as obtained from the ZEUS MHD simulation. Note that Venus was located essentially at the same heliolongitude as SolO but at $R = 0.722$ au (i.e., separated by just 0.06 au from SolO in radial distance; see Figure 8(a)). The four left panels in Figure 12(a) show, along the shock front and for the same time $dt = 33.4$ hr, the shock parameters (compression ratio, shock speed, obliquity angle θ_{Bn}) and the calculated local maximum energy at which particles are accelerated (using Equation (15) in J. Hu et al. 2017). Throughout the propagation of the shock, no magnetic connection was established between the shock and either STA or L1.

Figures 12(b)–(d) show the SEP simulation results at three locations: (b) PSP, (c) Venus (as a proxy for SolO), and (d) Earth. In particular, the left panels show the intensity-time profiles at (top) different energies from 2.2 to 100 MeV and (bottom) five integral channels; whereas the right panels show the energy spectra of particle fluences integrated over the whole duration of the simulation (black traces) or over different time intervals (colored traces).[40] Because very few particles reach Earth in the automatic ISWA run, we performed a new run with 50 times more test particles than the real-time model default setting, to generate the somewhat smoother results shown in Figure 12(d). All other input parameters were kept the same as the real-time simulations.

The intensity-time profiles at PSP and Venus in Figures 12(b) and (c) show similar trends as the actual observations displayed in Figure 10, including the arrival of the shock at SolO and the long intensity decay at both locations. At Earth, the simulation results (Figure 12(d)) display a similar intensity enhancement of SEPs between ~10 and 100 MeV as those measured in situ (Figure 11), with a time delay, even though Earth was located on the other side of the CME and did not establish magnetic connection with the simulated shock. Whereas the top left panel of Figure 12(d) shows some velocity dispersion of a few hours between the earlier arriving higher-energy particles and the lower-energy particles, this is not observed in the measured particle intensities (Figure 11). The elevated particle intensities observed prior to the onset of the M20 SEP event, resulting from preceding events, obscure the actual onset of the M20 SEP event. The low intensity of the M20 SEP event near Earth superimposed on this energy-dependent background made necessary the use of long-term averages to determine the onset times occurring between 3 and 4 hr after the flare occurrence where the velocity dispersion is difficult to discern. Additionally, the actual observed intensity profiles are affected by variations in the solar wind ambient medium, which is much more simplified in the simulations, where prior SEP intensities are absent, and SEP transport parameters follow prescribed energy dependences, making velocity dispersion effects more pronounced than in the actual measurements.

Because of the lack of magnetic field connection between L1 and the simulated shock, the arrival of energetic particles at Earth's location in the simulations is almost all caused by cross-field diffusion. The calculation of the perpendicular diffusion coefficient in the real-time iPATH model configuration is based on the nonlinear guiding center theory (A. Shalchi et al. 2010). The implementation of the cross-field diffusion in the real-time iPATH is the same as described in J. Hu et al. (2018) and Z. Ding et al. (2022). In the current real-time iPATH version, we also considered the turbulence correlation length scale to have a radial dependence of $\lambda_c \sim r^{1.1}$ based on recent PSP observations. The adopted turbulence level $\delta B^2/B^2$ was 0.47 at 1 au. The model calculated parallel mean free path for 10 MeV protons was 0.378 au with a corresponding perpendicular mean free path of 0.00367 au, and diffusion

[35] https://ccmc.gsfc.nasa.gov/tools/ISWA/

[36] Details about this version of iPATH can be found at https://ccmc.gsfc.nasa.gov/models/iPATH~2/.

[37] https://www.ap.smu.ca/~dclarke/zeus3d/version3.6/home.html

[38] https://kauai.ccmc.gsfc.nasa.gov/DONKI/view/CME/31034/1

[39] MHD simulation results and movies are available athttps://iswa.ccmc.gsfc.nasa.gov/iswa_data_tree/model/heliosphere/iPATH/2.X/CME/ZEUS/CME-shock-parameter/2024/05/ZEUS+iPATH_CME_20240520_053600_20240520_164336_CME-shock-parameters.gif for the leading edge CME parameters and https://iswa.ccmc.gsfc.nasa.gov/iswa_data_tree/model/heliosphere/iPATH/2.X/CME/ZEUS/CME-shock-parameter/2024/05/ZEUS+iPATH_CME_20240520_053600_20240520_161755_CME-shock-parameters.gif for the shock CME parameters.

[40] Raw data can be accessed from the ISWA data tree at https://iswa.ccmc.gsfc.nasa.gov/iswa_data_tree/model/heliosphere/iPATH/.

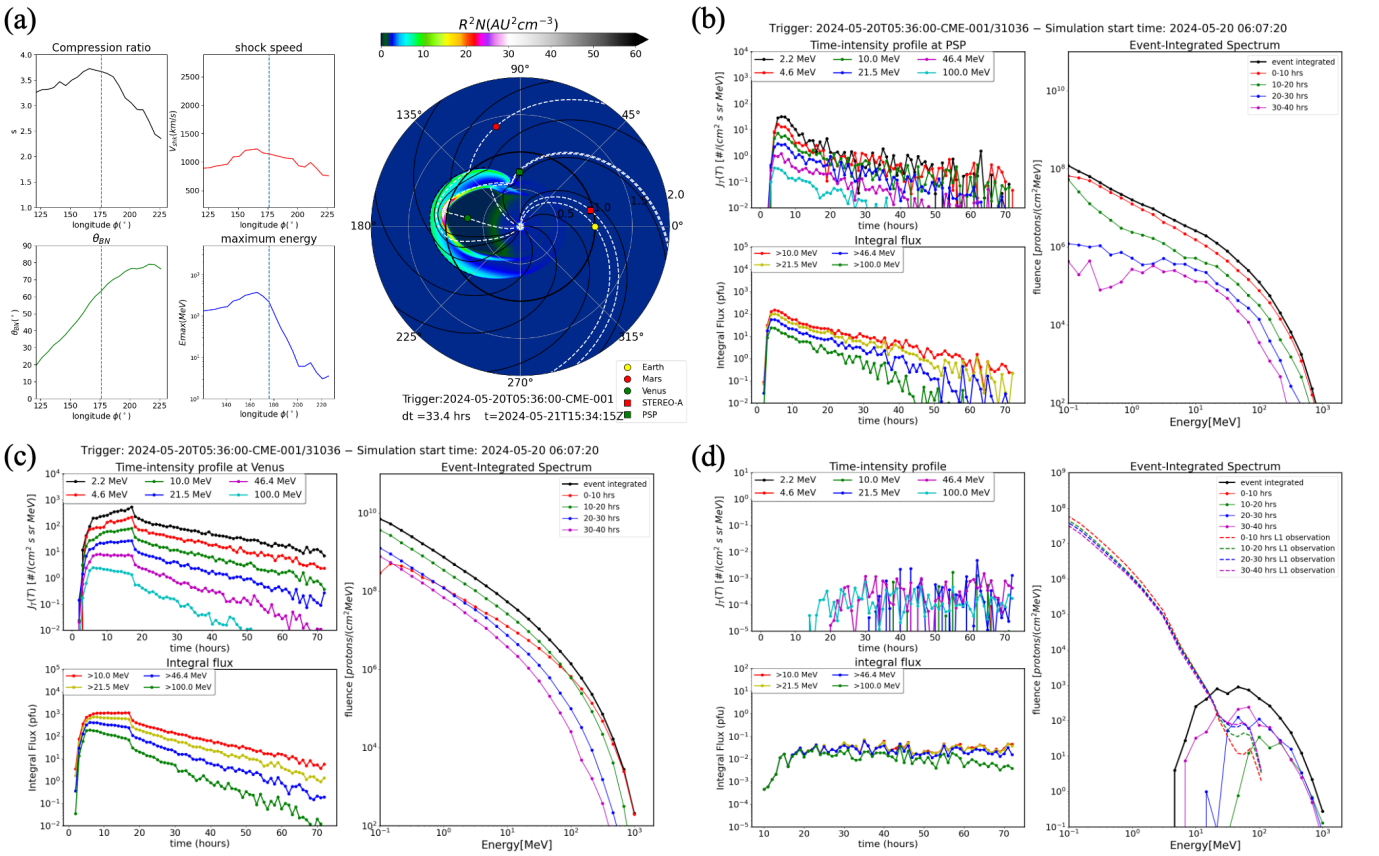

Figure 12. (a) Snapshot of iPATH simulation displaying the solar wind density contours (scaled by R^2) 33.4 hr after the simulation initiation (bluish-colored contour) and the parameters of the CME-driven shock along its front at the same time (four left panels showing clockwise density compression ratio, shock speed, maximum energy at which particles are accelerated, and shock normal angle with respect to the upstream magnetic field θ_{Bn}). In the density contour, the colored symbols indicate the location of Earth (yellow circle), STA (red square), Mars (red circle), Venus (green circle), and PSP (green square). Black- and white-dashed lines indicate IMF lines as obtained from the 2D MHD ZEUS simulation connecting each one of these objects with the Sun (white circle at the center). Longitudinal angles indicate the longitude in HEEQ coordinates. The vertical blue-dotted line in the four right panels indicate the longitude of the nose of the shock. (b)–(c) Proton intensity-time profiles at selected energies (top left) and at integral energy channels (bottom left) together with the proton energy spectra (right panels) integrated over the whole duration of the simulation (black traces) and over time intervals of 10 hr (colored traces), as obtained from the real-time iPATH simulation at (b) PSP, (c) Venus, which was very close to SolO, and (d) L1. Times indicate hours after the initiation of the simulation. The panel with the energy spectra at L1 contain the measured energy spectra for the first 40 hr of the SEP event as plotted in Figure C1(a).

coefficients scaled with radial distance using Equation (13) of Z. Ding et al. (2022).

In the right panel of Figure 12(d), we overplot the measured energy spectra based on the left panel of Figure C1. At energies $\lesssim$20 MeV, the measured fluences are dominated by the decaying intensities of earlier SEP events (Figure 11), whereas, at higher energies, the intensity-time profiles are similar to those plotted in the left panels of Figure 12(d), exhibiting a flattening below $\lesssim$100 MeV and absence of low-energy particles, which require longer times to diffuse across the field lines. In the simulations, particles arrive at Earth at approximately $dt \sim 10$ hr, whereas the onset of the SEP event at L1 occurred about ~3–4 hr after the onset of the eruption. This discrepancy is largely attributable to the inner boundary of the ZEUS model, in which the solar wind is initiated at $R = 0.05$ au (~10 $R_\odot$), and the shock forms even farther out. As a result, much of the early SEP acceleration occurring in the low corona is absent, and the iPATH SEP intensity onset time is always delayed by one to a few hours. Previous validation efforts have shown that iPATH tends to overestimate the maximum energies particles can reach. Consequently, the event-integrated fluence spectra at Earth are shifted to higher energies compared to observations. It should be emphasized that the real-time iPATH is an operations-focused code, designed to run without any human fine-tuning of the input parameters. Therefore, exact agreement between simulated and observed SEP profiles is not expected. Nonetheless, for this event, the simulation captures the overall trends of SEP intensities observed at multiple locations reasonably well, with the caveats above described. The results suggest that a significant enhancement of high-energy SEP intensities can occur even from CMEs originating on the far side of the Sun relative to the observer.

5.4. Influence of the IP Context

The M20 SEP event occurred after an intense period of solar activity during which multiple ICMEs were present in the IP medium (Figure 8). E. C. Roelof et al. (1992) suggested that magnetic structures, created by the superposition of outward-propagating plasma disturbances, for example, earlier CMEs, can inhibit the escape of low-energy ions, thereby forming energetic particle reservoirs in the inner heliosphere. Similarly, D. V. Reames et al. (1997), analyzing the spatial invariance of particle intensity-time profiles observed by multiple spacecraft, concluded that a "magnetic bottle" effect can occur,

wherein particles are quasi-trapped in the region behind the shock that accelerated them, experiencing intense scattering at the shock and mirroring in the converging fields near the Sun. The observation of the remarkably similar particle intensities during the decay phase of the M20 SEP event by all the spacecraft separated by ∼170° in longitude (Figure 4) suggests that confinement of particles may have occurred in the inner heliosphere. It is plausible that the merged CMEs wrapping around the Sun in Figure 8 were able to reflect and redistribute (via cross diffusion in this turbulent region) SEPs injected by the 2024 May 20 CME-driven shock over a wide longitudinal range, creating the energetic particle reservoir observed during the decay of the event and thus contributing to the SEP event observed at L1.

The onset of the SEP event at L1 and STA was observed with a delay of ∼3–4 hr with respect to the onset of the X16.5 flare. In 3 (4) hr, a 100 MeV proton traveling scatter-free can cover a distance of ∼9.3 au (∼12.4 au), whereas a 30 MeV proton can cover ∼5.4 au (∼7.2 au). Thus, these particles would have had sufficient time to reach the envelope formed by prior CMEs shown in Figure 8, redistribute in longitude, and return toward the Sun and be detected at L1. However, the gradual onset of the SEP event at both STA and L1 showed no evidence of such velocity dispersion across the different measured energies, implying that transport to a reflecting boundary and back to the spacecraft was unlikely to be scatter-free. This conclusion is further supported by the particle intensities measured by SOHO/ERNE being consistent with isotropic fluxes (see Appendix B). The IMF left behind the prior CMEs was likely highly complex (Figure 8) forcing particles to undergo multiple scattering and meandering paths, making the particle reflection and redistribution at the envelope of merged CMEs at large heliocentric distances difficult to meet the 3–4 hr delayed onset. This particle reflection and redistribution process may have contributed to spread SEPs in longitude and hence the observation of the particle reservoir displayed in Figure 4. However, the isotropic onset of the SEP event at L1 should be accompanied by diffusive gradual particle transport processes in a turbulent medium, not only in the merged-CME envelope.

In conclusion, it is likely that the extended decay of the M20 SEP event resulted from a combination of multiple cross-field diffusion processes, particle reflection and redistribution within the envelope formed by merged ICMEs, and drifts along the HCS. Notably, when considering only CME-driven shock acceleration and SEP transport via cross-field diffusion, Figures 12(b)–(c) show that high-energy particles arrive at L1, but the simulated high-energy intensities at PSP and SolO decay to preevent values within ∼2–3 days. In contrast, the measured SEP decays at PSP and SolO persisted for at least ∼10 days (Figure 10). Therefore, additional factors than those included in the iPATH modeling should have contributed to extend the SEP intensity decay. Apart from perpendicular SEP transport processes, HCS drifts, and reflection and redistribution of particles by the evolving boundaries of prior CMEs may have collectively contributed to the long-lasting decay observed at STA and L1 (Figure 11), but cross-field transport processes should have played a predominant role in the onset of the SEP event at STA and L1.

6. Summary

During the intense period of solar activity in 2024 May–June, the fleet of spacecraft distributed throughout the inner heliosphere (Figure 1) detected a series of large SEP events (Figure 4). Among these, the SEP event on 2024 May 20 stands out due to its high intensity as observed by well-connected spacecraft. It was associated with an EUV eruption and an X16.5 flare at W171 from Earth, as directly observed by instruments on board SolO (Figures 3 and 5). The CME associated with this far-side eruption (as seen from Earth) appeared as a fast halo CME in STA and SOHO coronagraph images, yet no clear signature of this eruption was detected on the Earth-facing disk of the Sun. Nevertheless, a long-lasting, high-energy (∼100 MeV) proton event with an energy spectrum flattening over the ∼30–80 MeV energy range (Figures 11 and C1) was detected by STA and near-Earth spacecraft, both positioned nearly diametrically opposite to the flare site. This event led to the formation of a long-lasting (∼2 week) high-energy particle reservoir extending over at least 170° in longitude as observed by SolO, PSP, and near-Earth spacecraft (Figure 4).

In addition, the M20 SEP event constituted the most intense Mars ground-level event recorded to date by MSL/RAD (A. Posner et al. 2025). The reconstruction of the shock driven by the CME on 2024 May 20 (Figure 6) reveals that Mars was magnetically connected to the nose of the CME-driven shock, consistent with the abrupt SEP onset, rapid peak, and subsequent gradual decay in intensities evident in Figure 2 of A. Posner et al. (2025) or Figure 1 in I. Mitrofanov et al. (2025) regarding the production of neutrons on the Martian surface. Similarly, PSP established magnetic connection westward of the nose of the shock, and as the shock expanded, the connection moved even more westward along the shock front, with only the western flank of the shock intercepting the spacecraft. SolO was initially connected to the eastern flank of the shock, but later, it connected to the shock nose when it arrived at the spacecraft. The intensity-time profiles observed at these locations (Figure 10) are consistent with the evolution of the spacecraft–shock magnetic connection. In contrast, the magnetic connections of STA and L1 with the shock, as determined by the geometric reconstruction shown in Figure 6, appear insufficient to explain the long-lasting high-energy particle intensity observed from this far-side eruption.

The observation of high-energy SEP events from far-side eruptions is not unprecedented. For example, (i) H. W. Dodson & E. R. Hedeman (1969) and J. A. Lockwood (1968) argued that the origin of GLE-16 on 1967 January 28 (with ∼3 GeV protons arriving at Earth) was located at ∼W155; (ii) E. W. Cliver (1982) concluded that GLE-23 on 1971 September 1 (with ∼2 GeV protons arriving at Earth) originated from ∼W120; (iii) H. Debrunner et al. (1988) reasoned that the origin of GLE-39 on 1984 February 16 (with ∼1 GeV protons arriving at Earth) was located at ∼W130; (iv) E. W. Cliver et al. (2005) attributed the origin of the SEP event on 2001 August 16 (with ∼400 MeV protons arriving at Earth) to a source located at ∼W180. These studies assumed that the most AR on the visible side of the Sun was the origin of the SEP event as it rotated beyond the west limb of the Sun. At lower energies, E. W. Cliver et al. (1995) used data from the Interplanetary Monitoring Platform-8 and the two Helios spacecraft to determine that the most intense 13–25 MeV proton events could be observed all around the Sun. Similarly,

I. G. Richardson et al. (2014, 2026), using >25 MeV proton measurements from SOHO, STA, and STEREO-Behind, determined that SEPs may be detected at all longitudes relative to the solar eruption. An extreme case was the SEP event on 2011 November 3, when >100 MeV protons were observed near Earth from a solar eruption at E152 (R. Gómez-Herrero et al. 2015).

Although high-energy SEP events from far-side eruptions are not uncommon, the M20 SEP event was exceptional because the distribution of spacecraft on 2024 May 20 (Figure 1) allowed for the location of the parent AR and confirmed that the effects of the solar eruption from this AR were limited to the far side of the Sun without clear evidence of EUV signatures on the Earth-facing side of the Sun. Additionally, the event was isolated from other solar eruptions, the elevated $\gtrsim$100 MeV proton intensities at L1 were observed for more than ~2 weeks with a flattening of the energy spectrum over the 30–80 MeV energy range, and an energetic particle reservoir spanning at least 170° in longitude was formed. These characteristics made the M20 SEP event propitious for the analysis of the mechanisms responsible for spreading SEPs in the inner heliosphere.

The arrival of SEPs at L1 likely involved a combination of particle transport and injection processes. While the fast halo CME was capable of driving a shock that efficiently accelerated particles to very high ($\gtrsim$100 MeV) energies, the geometric reconstruction of the shock suggests that STA and L1 were poorly connected to the shock (if connection was established at all). Even if the shock reconstruction was not entirely correct, and the flank of the shock was able to accelerate ~100 MeV protons and inject them onto field lines directly connected to L1 and STA, the prolonged decay of high-energy proton intensities at these two locations challenges the scenario in which a continuously connected shock alone supplied all the observed particles throughout the event. The S-web configuration may have contributed to broadening the longitudinal spread of particles and then extending the SEP decay, particularly when particles drifting along the HCS eventually reached STA and L1. Similarly, reflection and redistribution of particles by merged CMEs beyond 1 au may have prolonged the decay of the SEP event and contributed to the observation of the energetic particle reservoir. The onset of the SEP event at STA and L1 consistent with isotropic fluxes and with a 3–4 hr delay with respect to the far-side solar eruption suggests that transport processes determined the SEP arrival at these locations. Cross-field transport simulations provide an explanation for both the spread of particles in longitude and the flattening of the energy spectra at high energies, but they alone cannot account for the observed long-lasting decay at all spacecraft, unless transport and acceleration parameters are conveniently modified. A combination of processes (including particle acceleration at broad CME-driven shocks, cross-field transport, drifts along the HCS, and reflection/redistribution in CME-driven structures) likely contributed to the observed signatures of the M20 SEP event near Earth, with cross-field transport playing a particularly prominent role in the arrival of SEPs at L1 and STA.

Acknowledgments

We thank NASA and ESA for their support of the space missions whose data were used in this paper. Solar Orbiter is a mission of international cooperation between ESA and NASA, operated by ESA. SOHO is a mission of international cooperation between ESA and NASA, operated by NASA. STEREO is the third mission in NASA Solar Terrestrial Probes program. SDO is a mission of the NAS. Living With a Star Program. ACE is a mission of the NASA Explorer Program. Wind is a mission of the NASA Heliophysics System Observatory. PSP was designed, built, and is now operated by the Johns Hopkins Applied Physics Laboratory as part of NAS. Living with a Star (LWS) program (contract NNN06AA01C). Data used in this paper can be downloaded from https://soar.esac.esa.int/soar/, https://cdaweb.gsfc.nasa.gov/, https://stereo-ssc.nascom.nasa.gov/, and https://sdo.gsfc.nasa.gov/. The IS⊙IS data and visualization tools are available at https://spacephysics.princeton.edu/missions-instruments. We acknowledge use of the SOHO/LASCO CME catalog generated and maintained at the CDAW Data Center by NASA and The Catholic University of America in cooperation with the Naval Research Laboratory. We acknowledge use of the HELIO4CAST ICME catalog (ICMECAT) generated and maintained at the Austrian Space Weather Office (https://helioforecast.space/). Simulation results have been provided by the Community Coordinated Modeling Center (CCMC) at Goddard Space Flight Center through their publicly available simulation services (https://ccmc.gsfc.nasa.gov; ENLIL - David_Lario_051925_SH_2). The WSA model was developed by N. Arge now at NASA GSFC, and the ENLIL model was developed by D. Odstrcil now at GMU. D.L. and I. G.R. acknowledge support from NAS. Living With a Star (LWS) program NNH19ZDA001NLWS, the Guest Investigator Program NNH23ZDA001NHGIO (80NSSC24K0555), and NASA Space Weather Center of Excellence program under award 80NSSC23M0191 (CLEAR). D.L. acknowledges support from the Strategic Capability project under NASA grant 80NSSC22K0892 (SCEPTER). I.G.R. also acknowledges support from the ACE mission. Work at the University of Kiel was supported by the German Federal Ministry of Economic Affairs and Energy and the German Space Agency (Deutches Zentrum für Luft- und Raumfahrt, e.V., (DLR)), grant number 50OT2002. R.Y.K. acknowledges support by basic research funding from the Korea Astronomy and Space Science Institute (KASI; KASI2025185005). A.A. acknowledges the project PID2022-136828NB-C41 that received financial support from MICIU/AEI/10.13039/501100011033 and FEDER, UE; the support from grant CEX2024-001451-M funded by MICIU/AEI/10.13039/501100011033; and the Departament de Recerca i Universitats of Generalitat de Catalunya through grant 2021SGR 00679.

Appendix A
Comparison between Observed In Situ Magnetic Polarities and Estimated Magnetic Connectivity

In this section, we compare the magnetic field polarity observed in situ by each spacecraft during the M20 SEP event with the polarity of the regions where the different methods described in Section 4.2 estimate that each spacecraft established magnetic connection.

The left panel of Figure 10 shows that the magnetic field observed by SolO pointed mostly outward, although with large out-of-the ecliptic excursions. The only exceptions occurred during the periods immediately before and after the passage of the IP shocks on May 21 and 23. Table 3 and Figure 7 indicate that all connectivity methods estimated the SolO magnetic

footpoint to be located in a region of outward magnetic field polarity, in agreement with the in situ observations.

The right panel of Figure 10 shows that, during the onset of the SEP event, PSP observed an outward IMF polarity until 23:35 UT on 2024 May 21, when the field polarity switched to inward (red, vertical dotted line). The top panel of Figure 7 shows that the PSP footpoint derived from the Parker+PFSS method (open purple circle) agrees with this outward polarity, whereas the footpoint using ADAPT/WSA (solid purple circle) does not. The bottom panel of Figure 7 shows that PSP location projected to 5 $R_{\odot}$ was close to the HCS, transitioning from an outward to an inward polarity region. The HCS crossing at PSP was observed in situ at 23:35 UT on May 21 in close agreement with the projection of the HCS shown in Figure 7 when radially mapped from $R = 5\ R_{\odot}$ to $R = 0.74$ au.

Figure 11 shows that the field polarity observed by STA and ACE was mostly outward, but with multiple out-of-the-ecliptic excursions. The exception occurred on May 20 at STA, when the field was mostly radially inward ($\phi \sim 180°$). The top panel of Figure 7 shows that both STA and ACE were connected to an inward polarity region at CL $\sim$ 240°. The bottom panel indicates that both L1 and STA were located in the direction of the HCS that, considering the transit time from 5 $R_{\odot}$ to 1 au at 400 km s^{-1}, should be observed $\sim$4 days later. This is consistent with the field polarity changes observed in situ on May 24, although no clear change to a different field sector was observed.

Note that the different methods used to estimate the magnetic connectivity assume a Parker spiral IMF configuration at some height above the solar surface. For the period of the M20 SEP event, this assumption should be considered a strong approximation and not necessarily valid, owing to the presence of numerous transient structures in the IP medium (see Figure 8) that likely influenced the actual IMF configuration.

Appendix B
Anisotropies

SolO/EPD/HET consists of four apertures (north, south, Sun, asun) covering four viewing directions to the north and south of the ecliptic, along the nominal Parker spiral to the Sun, and along the nominal Parker spiral away from the Sun, respectively (see Figure 4 in J. Rodríguez-Pacheco et al. 2020). These four apertures allow us to analyze the energetic particle anisotropies at the three-axis, stabilized SolO. The pitch angle coverage by these four apertures depends on the orientation of the magnetic field with respect to these apertures. Figure B1(a) shows the 37.9–41.2 MeV proton intensities measured in each one of the SolO/EPD/HET apertures during the time interval May 20–22, whereas Figure B1(b) shows the pitch angle coverage of each one of these apertures. The green arrow in Figure B1(a) indicates the time of the onset of the X16.5 flare observed at SolO (Figure 3) but shifted back in time to the Sun (i.e., at 05:05 UT). The first 37.9–41.8 MeV protons were observed at $\sim$05:35 UT in the Sun aperture, then at the north aperture, and later in the south and asun apertures. A 41.8 MeV proton takes about $\sim$22.5 minutes to reach SolO propagating along the radial distance or $\sim$23.8 minutes along a Parker spiral IMF line in a $\sim$509 km s^{-1} solar wind assuming a scatter-free propagation and a pitch angle of 0°. The observed $\sim$30 minute delay may result from different transport conditions, different IMF topology, a delayed injection, or the fact that none of the EPD/HET apertures detected particles with small pitch angles. The orientation of the IMF measured by SolO (Figure 10) at the onset of the SEP event showed outward polarity with strong out-of-the-ecliptic components, implying that the Sun and north apertures detected small pitch angles but still $\gtrsim$45°. A first intensity peak was observed at $\sim$06:40 UT with the higher intensities in the north and Sun apertures. However, the maximum phase of the SEP event at these energies was dominated by the intensities in the south aperture, until about $\sim$13:00 UT on May 20 when the intensities decreased and became isotropic. Clearly, IP structures affected the arrival of particles throughout the rising phase of the M20 SEP event. The approaching arrival of the shock observed at 08:09 UT on May 21 led to an anisotropic increase of the proton intensities (starting at about $\sim$04:00 UT on May 21 as indicated by the vertical blue-dashed line in Figures B1(a)–(b)), with higher intensities in the Sun and north apertures. Note that, in this period prior to the shock arrival, the magnetic field displayed strong oscillations similar to those observed throughout the shock downstream region and during the ICME sheath region. Isotropic fluxes were observed during the decrease of the particle intensities observed after the shock, the passage of the ICME, and throughout the decay phase of the SEP event.

PSP/EPI-Hi/HET consists of two apertures A and B pointing approximately $\sim$20° and $\sim$220° from the Sun, respectively (see Figure 18 in D. J. McComas et al. 2016). Figure B1(c) shows the 38.0–45.2 MeV proton intensities measured in each one of these two apertures, whereas Figure B1(d) shows the pitch angle coverage of these two apertures. Note that during this period the spacecraft roll angle was constant, so that changes in the pitch angle were not due to spacecraft maneuvers, but to changes in the IMF orientation. The outward IMF polarity during the onset of the event (Figure 10) led HET-A to measure small pitch angles. The green arrow in Figure B1(c) indicates the time of the onset of the X16.5 flare (Figure 3) shifted back to the Sun. The onset of the event was observed first at HET-A (about $\sim$36 minutes after the green arrow) and about $\sim$3 minutes later in the HET-B aperture. A 45 MeV proton takes about 20.5 minutes to travel scatter-free along the radial distance up to PSP, or 21.6 minutes for a distance of 0.83 au (that would correspond to the length of a Parker spiral field line from the Sun to PSP with a solar wind speed of 500 km s^{-1}). The HET-A proton intensities were larger than those from HET-B throughout the rising and maximum phases of the SEP event, and even during the decaying phase up to approximately $\sim$18:00 UT on May 20 when fluxes became isotropic. The black, vertical dotted line at 03:00 UT on May 21 indicates the decrease of high-energy ($\gtrsim$13 MeV) proton intensities and increase at lower energies (Figure 10) that did not coincide with any clear discontinuity in the measured IMF. The passage of the shock at 17:45 UT on May 21 yielded an increase in the high-energy proton intensities but not a clear change in the anisotropies. The red, vertical dotted line at 23:35 UT on May 21 indicates a magnetic sector boundary crossing at 23:35 UT on May 21 with polarity changing from outward to inward but no changes in the already decreasing fluxes. The decrease of the particle intensities at these energies throughout the decay phase of the M20 SEP event was essentially isotropic.

Figure B2 shows the proton anisotropies as observed by SOHO/ERNE/HED. The view cone of the instrument is divided

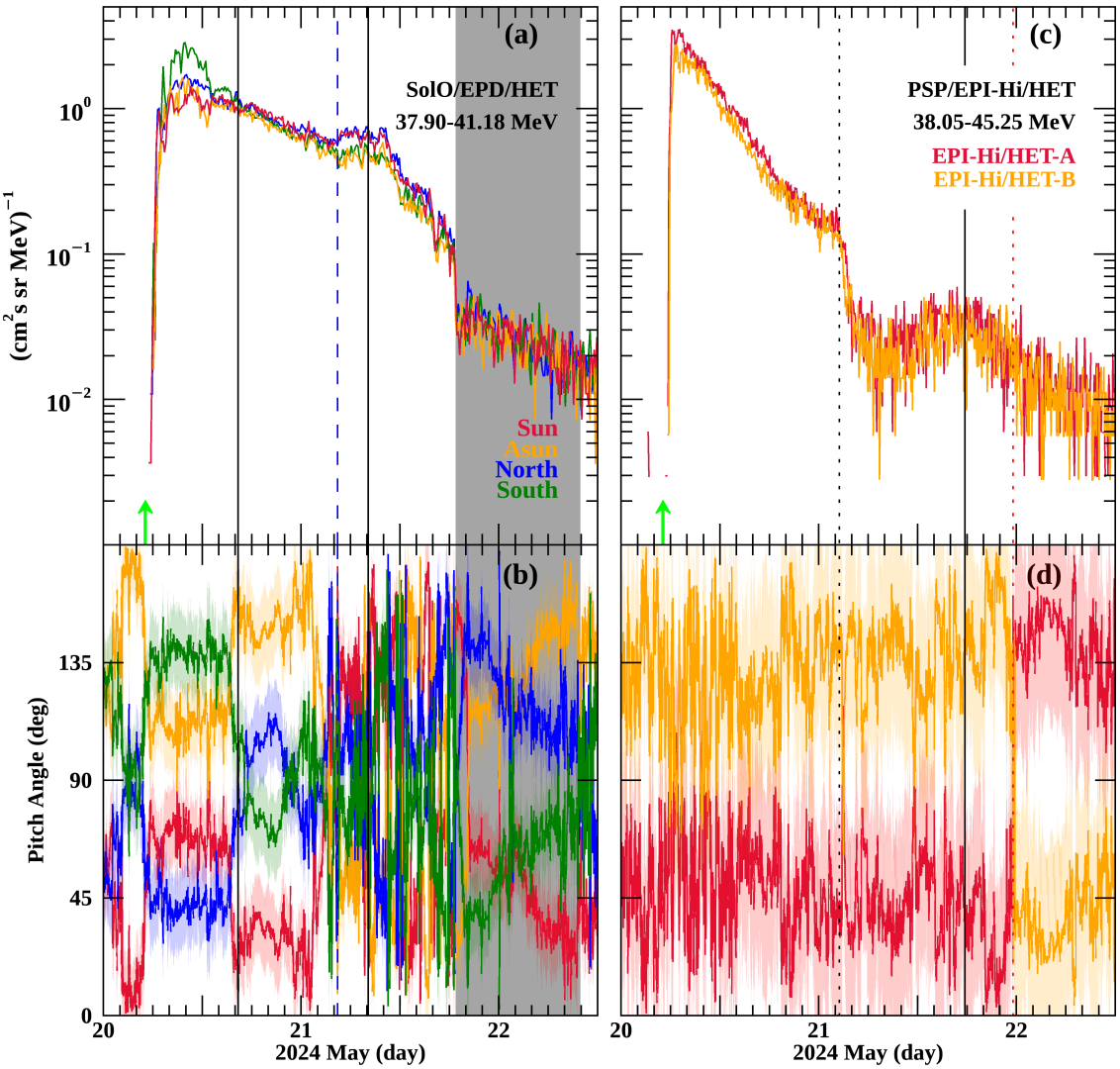

Figure B1. Left column: time evolution of (a) 37.9–41.2 MeV proton intensities measured in each one of the four SolO/EPD/HET apertures, and (b) pitch angle coverage scanned by the four SolO/EPD/HET apertures. Right column: time evolution of (c) 38.0–45.2 MeV proton intensities measured in each one of the apertures of PSP/EPI-Hi/HET, and (d) pitch angle coverage scanned by the two PSP/EPI-Hi/HET apertures. The green arrow in panels (a) and (b) indicate the time of the onset of the X16.5 flare (Figure 3) shifted back in time to the Sun.

into five segments: the central segment (close to the zenith of the detector) directed toward the nominal IMF Parker spiral direction, and four sectors looking above the ecliptic, below the ecliptic, toward the Sun, and toward the west (see Figure 7 in L. Kocharov et al. 2023). Figure B2(a) shows the 28–54 MeV proton intensities measured in each one of these five sectors from May 12 to June 12. This period covers the three >100 MeV proton intensity increases indicated by red dots as described in Section 3 (see Figure 2). With the exception of the onset and peak phases of the SEP events on May 13 and June 8, the intensities measured by SOHO/ERNE/HED were mostly isotropic. In order to characterize the asymmetries of the proton intensity within the HED viewing cone, two indices defined as $A_{\mathrm{Above-Below}} = (I_{\mathrm{Above}} - I_{\mathrm{Below}})/(I_{\mathrm{Above}} + I_{\mathrm{Below}})$ and $A_{\mathrm{Sun-West}} = (I_{\mathrm{Sun}} - I_{\mathrm{West}})/(I_{\mathrm{Sun}} + I_{\mathrm{West}})$ are plotted in Figure B2(b), indicating the north–south asymmetry and the east–west asymmetry of the proton intensity in the instrument's viewing cone. Figure B2(c) shows the statistical significance of these anisotropy indices, showing that during the onset of the SEP events on May 13 and June 8 the anisotropies were large and significant, whereas during the M20 SEP event the indices variations were insignificant around zero. Therefore, the proton anisotropies throughout the M20 SEP event at L1 were consistent with isotropic fluxes.

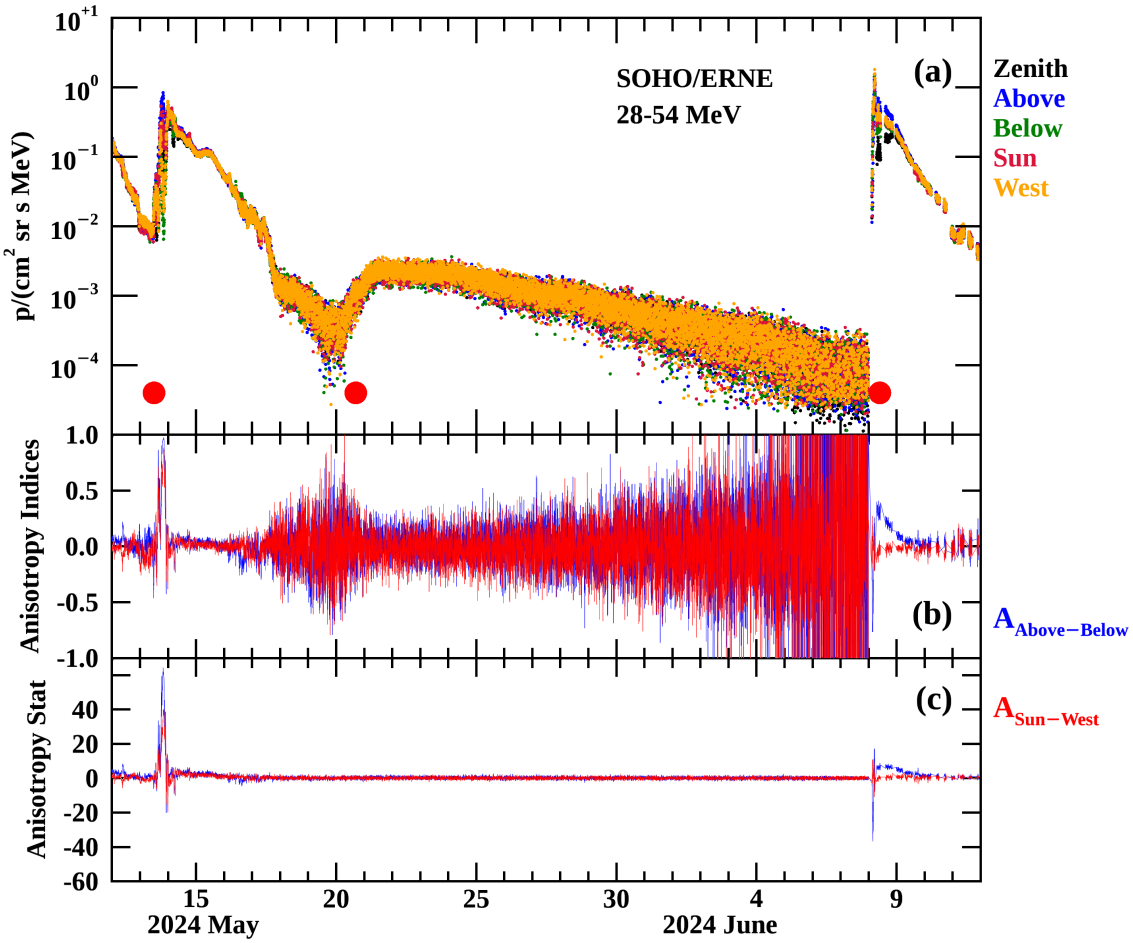

Figure B2. (a) Time profiles of the 28–54 MeV proton intensities measured in the five sectors of SOHO/ERNE. (b) Anisotropy indices $A_{\mathrm{Above-Below}}$ and $A_{\mathrm{Sun-West}}$, computed as defined in the text using the sectored intensities plotted in the top panel, and (c) statistical significance of the anisotropy indices. The red dots in panel (a) indicate the occurrence of the most energetic SEP events as identified in Figure 2.

Appendix C
Ion Energy Spectra at L1 and STA

Figure C1 shows the evolution of the ion energy spectra during the M20 SEP event as observed from (a) L1 and (b) STA. We use 10 hr averages of the ion intensities measured by (a) ACE/EPAM/LEMS120, SOHO/EPHIN, and SOHO/ERNE, and (b) STA/SEPT, STA/LET, and STA/HET (spin-averaged and omnidirectional intensities from ACE/EPAM/LEMS120 and STA/SEPT were, respectively, used). The black symbols indicate intensities for a period of 10 hr prior to the onset of the event, whereas the dark-blue symbols consider a period already including the onset of the event. Particle intensities below $\lesssim$15 MeV are dominated by the decaying intensities from prior SEP events (see Figure 11). A flattening of the energy spectrum over the energy range ~30–80 MeV (indicated by the horizontal green arrows) was observed whereas the intensities gradually decreased up to early June when the intensities either reached the STA/HET sensitivity threshold in the case of STA or continued to decreased in the case of SOHO/ERNE until June 8 when GLE-75 occurred (Figure 4). Energy spectra in Figure C1 are only plotted until May 28 because new SEP injections contributed to the low-energy intensity profiles (Figure 11).

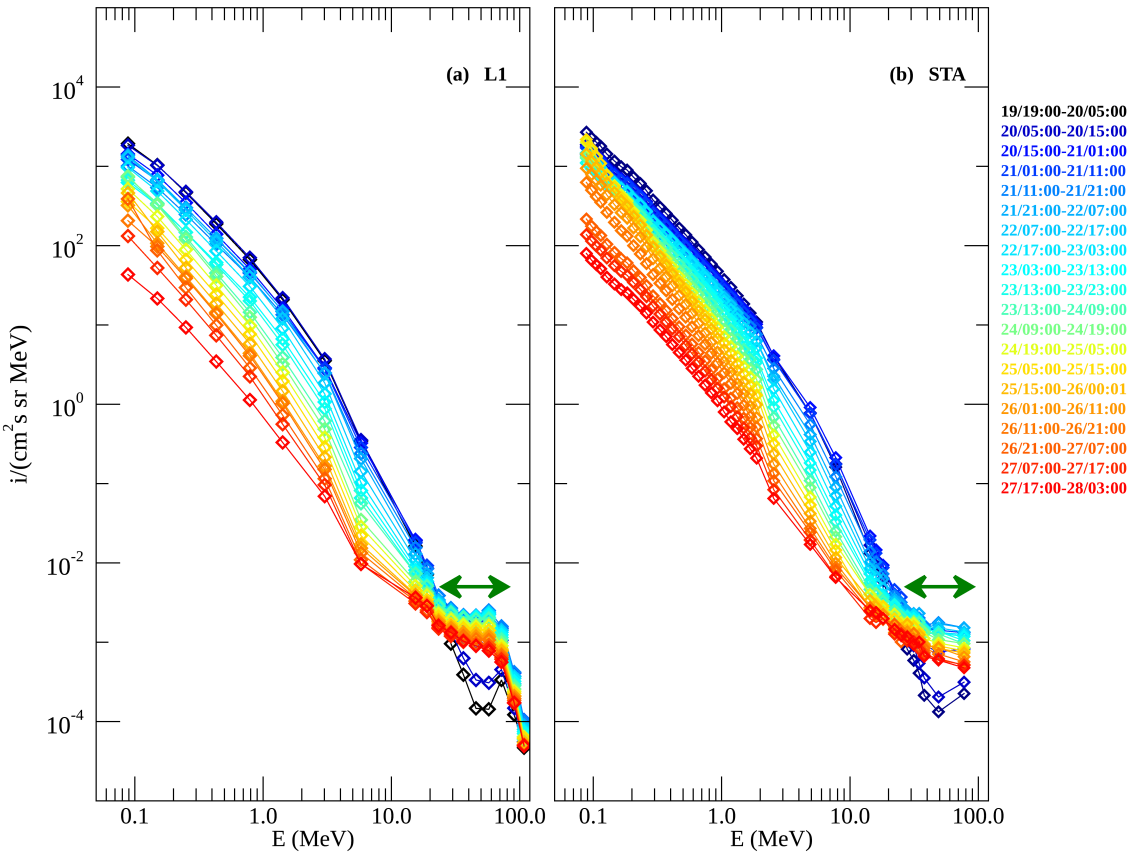

Figure C1. 10 hr average energy spectra combining different instruments on (a) ACE and SOHO, and (b) STA. Black symbols indicate preevent intensities dominated by instrumental background at high energies, whereas at low energies they are dominated by prior SEP events. The green horizontal arrows indicate the energy range (∼20–80 MeV) over which the flattening in the energy spectra was observed as intensities decreased over time.

ORCID iDs

D. Lario https://orcid.org/0000-0002-3176-8704
J. Hu https://orcid.org/0000-0001-7870-8883
L. A. Balmaceda https://orcid.org/0000-0003-1162-5498
R. Y. Kwon https://orcid.org/0000-0002-2106-9168
S. Wallace https://orcid.org/0000-0002-1091-4688
D. E. da Silva https://orcid.org/0000-0001-7537-3539
M. L. Mays https://orcid.org/0000-0001-9177-8405
V. Krupar https://orcid.org/0000-0001-6185-3945
F. Carcaboso https://orcid.org/0000-0003-1758-6194
A. Warmuth https://orcid.org/0000-0003-1439-3610
M. Z. Stiefel https://orcid.org/0000-0002-8538-3455
L. Y. Khoo https://orcid.org/0000-0003-0412-1064
I. G. Richardson https://orcid.org/0000-0002-3855-3634
P. Kühl https://orcid.org/0000-0002-3758-9272
R. F. Wimmer-Schweingruber https://orcid.org/0000-0002-7388-173X
R. Vainio https://orcid.org/0000-0002-3298-2067
W. Liu https://orcid.org/0000-0002-2873-5688
A. Aran https://orcid.org/0000-0003-1539-7832
E. Paouris https://orcid.org/0000-0002-8387-5202
M. R. Kane https://orcid.org/0009-0005-7792-2585
C. O. Lee https://orcid.org/0000-0002-1604-3326
C. Sasso https://orcid.org/0000-0002-5163-5837
C. N. Arge https://orcid.org/0000-0001-9326-3448
S. I. Jones https://orcid.org/0000-0001-9498-460X
J. Verniero https://orcid.org/0000-0003-1138-652X
A. E. Niemela https://orcid.org/0000-0002-3746-9246
T. S. Horbury https://orcid.org/0000-0002-7572-4690
M. Maksimovic https://orcid.org/0000-0001-6172-5062

References

Acuña, M. H., Curtis, D., Scheifele, J. L., et al. 2008, SSRv, 136, 203
Acuña, M. H., Ogilvie, K. W., Baker, D. N., et al. 1995, SSRv, 71, 5
Antonucci, E., Romoli, M., Andretta, V., et al. 2020, A&A, 642, A10
Arge, C. N., Henney, C. J., Koller, J., et al. 2010, AIPC, 1216, 343
Arge, C. N., Luhmann, J. G., Odstrcil, D., Schrijver, C. J., & Li, Y. 2004, JASTP, 66, 1295
Augusto, C. R. A., Navia, C. E., de Oliveira, M. N., et al. 2019, PASP, 131, 024401
Bale, S. D., Goetz, K., Harvey, P. R., et al. 2016, SSRv, 204, 49
Blinder, C. 2025, EOS, 106, 357
Bougeret, J. L., Goetz, K., Kaiser, M. L., et al. 2008, SSRv, 136, 487
Bougeret, J. L., Kaiser, M. L., Kellogg, P. J., et al. 1995, SSRv, 71, 231
Brueckner, G. E., Howard, R. A., Koomen, M. J., et al. 1995, SoPh, 162, 357
Burton, R. K., McPherron, R. L., & Russell, C. T. 1975, JGR, 80, 4204
Cane, H. V., Reames, D. V., & von Rosenvinge, T. T. 1988, JGR, 93, 9555
Chamberlin, P. C., Woods, T. N., Eparvier, F. G., & Jones, A. R. 2009, SPIE, 7438, 743802
Cliver, E. W. 1982, SoPh, 75, 341
Cliver, E. W., Kahler, S. W., Neidig, D. F., et al. 1995, ICRC, 4, 257
Cliver, E. W., Thompson, B. J., Lawrence, G. R., et al. 2005, ICRC, 1, 121
Cohen, C. M. S., Christian, E. R., Cummings, A. C., et al. 2021, A&A, 656, A29
Collier, H., Limousin, O., Xiao, H., et al. 2024, ITNS, 71, 1606
da Silva, D. E., Wallace, S., Arge, C. N., & Jones, S. 2023, SpWea, 21, e2023SW003554
Debrunner, H., Flueckiger, E., Graedel, H., Lockwood, J. A., & McGuire, R. E. 1988, JGR, 93, 7206
Dikpati, M., Korsós, M. B., Norton, A. A., et al. 2025, ApJ, 988, 108
Ding, Z., Wijsen, N., Li, G., & Poedts, S. 2022, A&A, 668, A71

Ding, Z.-Y., Li, G., Hu, J.-X., & Fu, S. 2020, RAA, 20, 145
Dodson, H. W., & Hedeman, E. R. 1969, SoPh, 9, 278
Domingo, V., Fleck, B., & Poland, A. I. 1995, SoPh, 162, 1
Dresing, N., Gómez-Herrero, R., Klassen, A., et al. 2012, SoPh, 281, 281
Dröge, W., Kartavykh, Y. Y., Dresing, N., & Klassen, A. 2016, ApJ, 826, 134
Dröge, W., Kartavykh, Y. Y., Klecker, B., & Kovaltsov, G. A. 2010, ApJ, 709, 912
Fox, N. J., Velli, M. C., Bale, S. D., et al. 2016, SSRv, 204, 7
Galvin, A. B., Kistler, L. M., Popecki, M. A., et al. 2008, SSRv, 136, 437
Gold, R. E., Krimigis, S. M., Hawkins, S. E., III, et al. 1998, SSRv, 86, 541
Gómez-Herrero, R., Dresing, N., Klassen, A., et al. 2015, ApJ, 799, 55
Harten, R., & Clark, K. 1995, SSRv, 71, 23
Harvey, J. W., Hill, F., Hubbard, R. P., et al. 1996, Sci, 272, 1284
Hassler, D. M., Zeitlin, C., Wimmer-Schweingruber, R. F., et al. 2012, SSRv, 170, 503
Hayakawa, H., Ebihara, Y., Mishev, A., et al. 2025, ApJ, 979, 49
He, H. Q. 2021, MNRAS, 508, L1
Horbury, T. S., O'Brien, H., Carrasco Blazquez, I., et al. 2020, A&A, 642, A9
Howard, R. A., Moses, J. D., Vourlidas, A., et al. 2008, SSRv, 136, 67
Hu, J., Li, G., Ao, X., Zank, G. P., & Verkhoglyadova, O. 2017, JGRA, 122, 10,938
Hu, J., Li, G., Fu, S., Zank, G., & Ao, X. 2018, ApJL, 854, L19
Jarolim, R., Veronig, A. M., Purkhart, S., Zhang, P., & Rempel, M. 2024, ApJL, 976, L12
Jaswal, P., Sinha, S., & Nandy, D. 2025, ApJ, 979, 31
Kahler, S. W., & Reames, D. V. 2003, ApJ, 584, 1063
Kaiser, M. L., Kucera, T. A., Davila, J. M., et al. 2008, SSRv, 136, 5
Kasper, J. C., Abiad, R., Austin, G., et al. 2016, SSRv, 204, 131
Khuntia, S., Mishra, W., & Agarwal, A. 2025, A&A, 698, A79
Klein, K. L., Krucker, S., Lointier, G., & Kerdraon, A. 2008, A&A, 486, 589
Kocharov, L., Mishev, A., Riihonen, E., Vainio, R., & Usoskin, I. 2023, ApJ, 958, 122
Kollhoff, A., Kouloumvakos, A., Lario, D., et al. 2021, A&A, 656, A20
Kollhoff, A. L. 2025, PhD Thesis, Christian-Albrechts-Universität zu Kiel https://macau.uni-Kiel.de/receive/macau_mods_00006127
Kondrashova, N. M., Pasechnik, M. M., Osipov, S. M., & Pishkalo, M. I. 2024, OAP, 37, 112
Kontogiannis, I. 2024, A&A, 690, L10
Kontogiannis, I., Zhu, Y., Barczynski, K., et al. 2025, A&A, 704, A105
Kress, B. T., Rodriguez, J. V., Boudouridis, A., et al. 2021, SpWea, 19, e02750
Krucker, S., Hurford, G. J., Grimm, O., et al. 2020, A&A, 642, A15
Krupar, V., Kruparova, O., Szabo, A., et al. 2024, ApJ, 961, 88
Kruparova, O., Krupar, V., Szabo, A., et al. 2024, ApJL, 970, L13
Kunow, H., Wibberenz, G., Green, G., Müller-Mellin, R., & Kallenrode, M.-B. 1991, in Physics of the Inner Heliosphere II, Physics and Chemistry in Space, Vol. 21, ed. R. Schwenn & E. Marsch (Springer), 243
Kwak, Y.-S., Kim, J.-H., Kim, S., et al. 2024, JASS, 41, 171
Kwon, R.-Y., Ofman, L., Olmedo, O., et al. 2013, ApJ, 766, 55
Kwon, R.-Y., & Vourlidas, A. 2017, ApJ, 836, 246
Kwon, R.-Y., Zhang, J., & Olmedo, O. 2014, ApJ, 794, 148
Lario, D. 2010, AIPC, 1216, 625
Lario, D., Kallenrode, M. B., Decker, R. B., et al. 2006, ApJ, 653, 1531
Lario, D., Kwon, R. Y., Richardson, I. G., et al. 2017a, ApJ, 838, 51
Lario, D., Kwon, R. Y., Balmaceda, L., et al. 2020, ApJ, 889, 92
Lario, D., Kwon, R. Y., Riley, P., & Raouafi, N. E. 2017b, ApJ, 847, 103
Lario, D., Raouafi, N. E., Kwon, R. Y., et al. 2014, ApJ, 797, 8
Lario, D., Roelof, E. C., Decker, R. B., & Reisenfeld, D. B. 2003, AdSpR, 32, 579
Lario, D., Sanahuja, B., & Heras, A. M. 1998, ApJ, 509, 415
Lemen, J. R., Title, A. M., Akin, D. J., et al. 2012, SoPh, 275, 17
Li, Y., Liu, X., Jing, Z., et al. 2024, ApJL, 972, L1
Liu, W., Sokolov, I. V., Zhao, L., et al. 2025, ApJ, 985, 82
Lockwood, J. A. 1968, JGR, 73, 4247
Luhmann, J. G., Curtis, D. W., Schroeder, P., et al. 2008, SSRv, 136, 117
MacNeice, P., Elliott, B., & Acebal, A. 2011, SpWea, 9, S10003
MacTaggart, D., Williams, T., & Aslam, O. P. M. 2025, JGRA, 130, e2024JA033462
Maksimovic, M., Bale, S. D., Chust, T., et al. 2020, A&A, 642, A12
Maksimovic, M., Souček, J., Chust, T., et al. 2021, A&A, 656, A41
Masson, S., Antiochos, S. K., & DeVore, C. R. 2013, ApJ, 771, 82
Masson, S., Démoulin, P., Dasso, S., & Klein, K. L. 2012, A&A, 538, A32
Mays, M. L., Taktakishvili, A., Pulkkinen, A., et al. 2015, SoPh, 290, 1775
McComas, D. J., Alexander, N., Angold, N., et al. 2016, SSRv, 204, 187
McKibben, R. B. 1972, JGR, 77, 3957
McKibben, R. B., Connell, J. J., Lopate, C., et al. 2003, AnGeo, 21, 1217
Millward, G., Biesecker, D., Pizzo, V., & de Koning, C. A. 2013, SpWea, 11, 57
Mitrofanov, I., Litvak, M., Sanin, A., et al. 2025, AcAau, 234, 734
Moradi, A., & Giacalone, J. 2022, ApJ, 932, 73
Moradi, A., & Giacalone, J. 2025, ApJ, 980, 182
Möstl, C., Isavnin, A., Boakes, P. D., et al. 2017, SpWea, 15, 955
Möstl, C., Weiss, A. J., Bailey, R. L., et al. 2020, ApJ, 903, 92
Müller, D., St. Cyr, O. C., Zouganelis, I., et al. 2020, A&A, 642, A1
Müller-Mellin, R., Böttcher, S., Falenski, J., et al. 2008, SSRv, 136, 363
Müller-Mellin, R., Kunow, H., Fleißner, V., et al. 1995, SoPh, 162, 483
O'Brien, T. P., & McPherron, R. L. 2000, JGR, 105, 7707
Odstrcil, D., Mays, M. L., Hess, P., et al. 2020, ApJS, 246, 73
Odstrcil, D., Riley, P., & Zhao, X. P. 2004, JGRA, 109, A02116
Odstrčil, D., Smith, Z., & Dryer, M. 1996, Geophys. Res. Lett., 23, 2521
Ogilvie, K. W., Chornay, D. J., Fritzenreiter, R. J., et al. 1995, SSRv, 71, 55
Owen, C. J., Bruno, R., Livi, S., et al. 2020, A&A, 642, A16
Paouris, E., Vourlidas, A., Georgoulis, M. K., Hess, P., & Stenborg, G. 2025, ApJ, 982, 194
Paouris, E., Vourlidas, A., Kouloumvakos, A., et al. 2023, ApJ, 956, 58
Papaioannou, A., Mishev, A., Usoskin, I., et al. 2025, SoPh, 300, 73
Pesnell, W. D., Thompson, B. J., & Chamberlin, P. C. 2012, SoPh, 275, 3
Poluianov, S., Mishev, A., Kryakunova, O., et al. 2025, SoPh, 300, 113
Posner, A., Richardson, I. G., & Strauss, R. D. T. 2024, SoPh, 299, 126
Posner, A., Richardson, I. G., & Zeitlin, C. J. 2025, SoPh, 300, 102
Razquin, A., Veronig, A. M., Dissauer, K., Podladchikova, T., & Jain, S. 2025, A&A, 699, A40
Reames, D. V. 1999, SSRv, 90, 413
Reames, D. V. 2021, Solar Energetic Particles. A Modern Primer on Understanding Sources, Acceleration and Propagation, 978 (Springer)
Reames, D. V. 2023, FrASS, 10, 1254266
Reames, D. V., Barbier, L. M., & Ng, C. K. 1996, ApJ, 466, 473
Reames, D. V., Kahler, S. W., & Ng, C. K. 1997, ApJ, 491, 414
Richardson, I. G., & Cane, H. V. 2010, SoPh, 264, 189
Richardson, I. G., von Rosenvinge, T. T., Cane, H. V., et al. 2014, SoPh, 289, 3059
Richardson, I. G., von Rosenvinge, T. T., St. Cyr, O. C., et al. 2026, SoPh, in press (arXiv:2601.09630)
Rochus, P., Auchère, F., Berghmans, D., et al. 2020, A&A, 642, A8
Rodríguez-García, L., Palmerio, E., Pinto, M., et al. 2025, A&A, 701, A13
Rodríguez-Pacheco, J., Wimmer-Schweingruber, R. F., Mason, G. M., et al. 2020, A&A, 642, A7
Roelof, E. C., Gold, R. E., Simnett, G. M., et al. 1992, GeoRL, 19, 1243
Romano, P., Elmhamdi, A., Marassi, A., & Contarino, L. 2024, ApJL, 973, L31
Rouillard, A. P., Pinto, R. F., Vourlidas, A., et al. 2020, A&A, 642, A2
Schatten, K. H. 1971, CosEl, 2, 232
Schatten, K. H. 1972, in NASA Special Publication, Vol. 308, Solar Wind, ed. C. P. Sonett, P. J. Coleman, & J. M. Wilcox (NASA), 44
Scherrer, P. H., Schou, J., Bush, R. I., et al. 2012, SoPh, 275, 207
Schonfeld, S., Henney, C. J., Jones, S. I., & Arge, C. N. 2024, AGUFM, 2024, SH22B
Schrijver, C. J., & Title, A. M. 2003, ApJL, 597, L165
Schwadron, N. A., Caplan, R. M., Linker, J. A., Palmerio, E., & Young, M. A. 2026, ApJ, 996, 109
Shalchi, A., Li, G., & Zank, G. P. 2010, Ap&SS, 325, 99
Smith, C. W., L'Heureux, J., Ness, N. F., et al. 1998, SSRv, 86, 613
Solanki, S. K., del Toro Iniesta, J. C., Woch, J., et al. 2020, A&A, 642, A11
Stiefel, M. Z., Kuhar, M., Limousin, O., et al. 2025, A&A, 694, A138
Stone, E. C., Frandsen, A. M., Mewaldt, R. A., et al. 1998, SSRv, 86, 1
Swalwell, B., Dalla, S., & Walsh, R. W. 2017, SoPh, 292, 173
Titov, V. S., Mikić, Z., Linker, J. A., Lionello, R., & Antiochos, S. K. 2011, ApJ, 731, 111
Torsti, J., Valtonen, E., Lumme, M., et al. 1995, SoPh, 162, 505
Veronig, A., Temmer, M., Hanslmeier, A., Otruba, W., & Messerotti, M. 2002, A&A, 382, 1070
von Rosenvinge, T. T., Reames, D. V., Baker, R., et al. 2008, SSRv, 136, 391
Wallace, S., Higginson, A. K., Simpson, D. G., et al. 2025, JGRA, 130, e2025JA033743
Wang, Y., & Qin, G. 2023, ApJ, 954, 81
Waterfall, C. O. G., Dalla, S., Laitinen, T., Hutchinson, A., & Marsh, M. 2022, ApJ, 934, 82
Waterfall, C. O. G., de Nolfo, G. A., Hutchinson, A., et al. 2025, ApJ, 991, 104
Wuelser, J.-P., Lemen, J. R., Tarbell, T. D., et al. 2004, SPIE, 5171, 111
Xiao, H., Maloney, S., Krucker, S., et al. 2023, A&A, 673, A142
Yashiro, S., Gopalswamy, N., Michalek, G., et al. 2004, JGRA, 109, A07105
Zhang, M., Cheng, L., Zhang, J., et al. 2023, ApJS, 266, 35
Zhang, M., Qin, G., & Rassoul, H. 2009, ApJ, 692, 109